Microstructural deformation of zircon during impact metamorphism

Plan, Anders

2025

LITHOLUND THESES 42

Microstructural Deformation of Zircon During Impact Metamorphism

ANDERS PLAN
LITHOSPHERE AND BIOSPHERE SCIENCE | DEPARTMENT OF GEOLOGY | LUND UNIVERSITY 2025

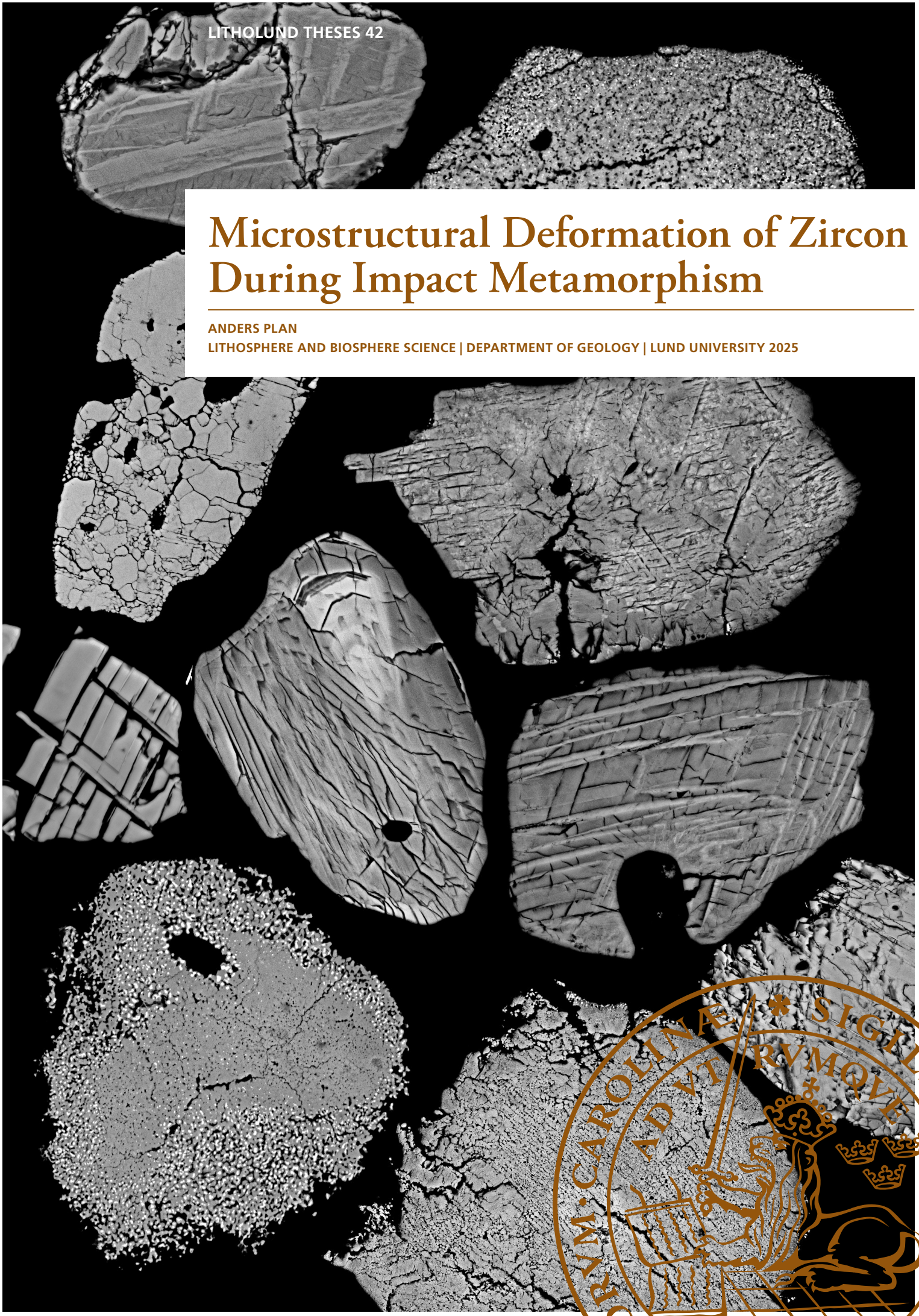

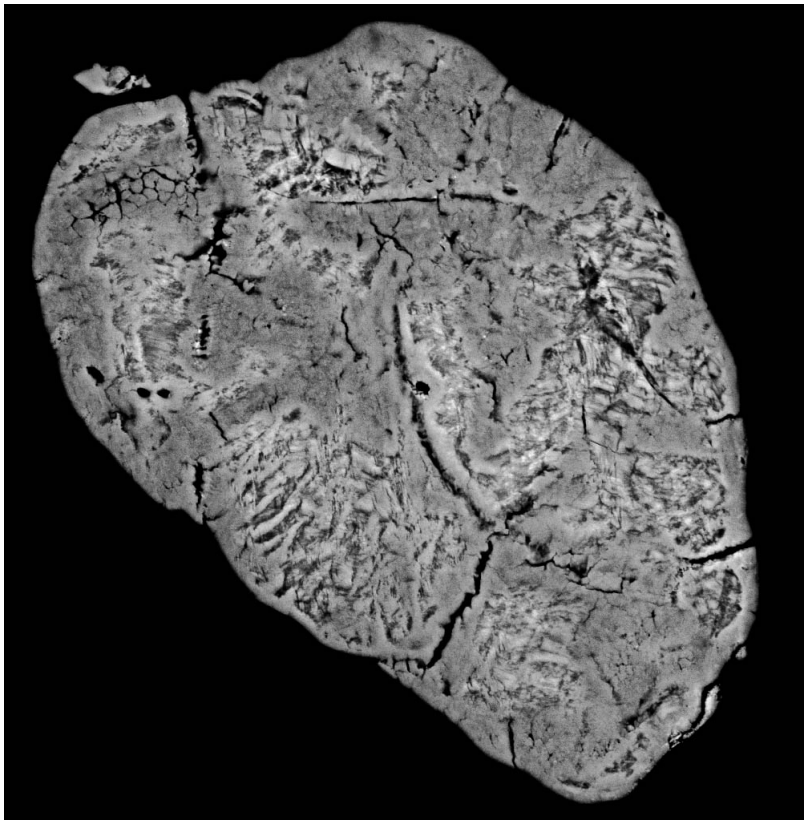

Printed by Media-Tryck, Lund 2019 NORDIC SWAN ECOLABEL 3041 0903

Lithosphere and Biosphere Science
Department of Geology
Lund University
Sölvegatan 12
SE-223 62 Lund, Sweden
Telephone +46 46 222 78 80

ISSN 1651-6648
ISBN 978-91-87847-88-2

LITHOLUND THESES 42

Microstructural Deformation of Zircon During Impact Metamorphism

Anders Plan

LUND UNIVERSITY

Lithosphere and Biosphere Science
Department of Geology

DOCTORAL DISSERTATION
by due permission of the Faculty of Science, Lund University, Sweden.
To be defended at Geocentrum II, Sölvegatan 12, Lund, room Pangea, on the 16th of May 2025, at 13:15.

Faculty opponent
Prof. Dr. James Darling
University of Portsmouth

Cover picture: Scanning electron microscope composite images of various shocked zircon from the Rochechouart crater. Photography and design: Anders Plan

Thesis figures and illustration design: Anders Plan

Lithosphere and Biosphere Science
Department of Geology
Faculty of Science

ISBN 978-91-87847-88-2 (print)

ISBN 978-91-87847-89-9 (pdf)

ISSN 1651-6648

Printed in Sweden by Media-Tryck, Lund University, Lund 2025

Organization

LUND UNIVERSITY
Department of Geology
Sölvegatan 12
SE-223 62 Lund
Sweden

Author: Anders Plan

Document name

DOCTORAL DISSERTATION

Date of issue: 16th of May, 2025

Sponsoring organization

Title and subtitle: Microstructural Deformation of Zircon During Impact Metamorphism

Abstract

Impact craters are among the most pervasive geological features on solid bodies throughout the inner Solar System. The heavily cratered surface of the Moon offers a stark visual record of the Solar System's early history of intense bombardment, a record largely absents from Earth's dynamic surface. Despite having experienced a comparable flux of impact events over deep time, Earth's geological processes—plate tectonics, erosion, sedimentation, and biological overprint—have significantly obscured or obliterated much of this record. Today, fewer than 200 confirmed impact structures are known on our planet. However, Impact cratering is now firmly established as a fundamental geological process with far-reaching implications for planetary evolution. On Earth, the consequences of large-scale impacts extend beyond crustal modification. One Impact have been directly linked to profound shifts in the geobiosphere, the Chicxulub event at ~66 million years ago, which coincides with the Cretaceous–Paleogene mass extinction. Such events highlight the critical role that impact cratering has played in shaping not only planetary surfaces, but also the trajectory of life itself.

In addition to global consequences, impact events produce a distinct suite of mineralogical deformation features within the target rocks. The brief but intense pressures (>10–100 GPa) and temperatures (>1,000°C) gradients generated during hypervelocity impact are sufficiently high to induce permanent structural deformations in both rocks and minerals—a phenomenon known as impact metamorphism. These shock features are unique to impact cratering processes and are critical to confirming the impact origin of a structure but can also be used to reconstructing the conditions of crater formation. Studying shock metamorphic effects at the micro- and nanoscale allows for quantitative reconstruction of the impact process, including pressure-temperature calibration, and to understand the underlying deformation mechanisms. Importantly, the mineral zircon does not only record these extreme conditions, but also preserve geochronological information that can be utilized to constrain dates of impact events (e.g. through the U-Pb isotopic system). Understanding how zircon respond to various pressure-temperature conditions is therefore crucial.

The research presented in this thesis investigates how zircon responds to the extreme pressure-temperature conditions generated during hypervelocity impact events. Using a combination of high-resolution analytical techniques—scanning electron microscopy (SEM), electron backscatter diffraction (EBSD), Raman spectroscopy, and transmission electron microscopy (TEM)—zircon grains from the Rochechouart impact structure in France were examined in order to understand various deformation mechanisms, high-pressure phase transformations, and shock-induced recrystallization.

Paper I focuses on the preservation and diversity of reidite, a high-pressure polymorph of zircon. Five distinct reidite morphologies were here characterized, including three newly documented habits. These habits exhibit systematic crosscutting relationships, indicative that reidite can form during both compression and decompression during impact. The study also documents the first evidence of localized reversion of reidite to zircon, forming distinct microstructural textures, and providing new constraints on post-shock thermal conditions and insights to zircon → reidite → zircon phase transformation.

In Paper II, Raman spectroscopy was used to characterize spectral signatures of shocked zircon and reidite. The study identifies diagnostic spectral shifts associated with increasing shock intensity, revealing how strain is partitioned during both peak-pressure conditions and during the post-shock temperature excursion. Most importantly, this study highlights that potential misidentifications of reidite can occur. Erroneous interpretations arise from spectral interference by rare earth elements, which tend to overlap spectral signatures of reidite. A refined methodological framework is here proposed for distinguishing between various zircon polymorphs, improving the reliability of Raman spectroscopy in impact metamorphic studies.

Paper III explores the role of shear localization in driving solid-state recrystallization of zircon. Through EBSD and TEM analyses, the study outlines a sequence of microstructural transitions and evolution, from dislocation accumulation to the formation of granular neoblastic shear bands. The results show that dynamic recrystallization in zircon is facilitated by localized heating and intense strain, offering new insights into how zircon both deforms and recrystallizes under extreme pressure-temperature conditions.

Together, the three studies of this thesis provide a comprehensive view of how zircon records impact metamorphic conditions associated with the extreme pressures and temperatures associated with impact cratering. The findings thus offer new tools for interpreting pressure-temperature histories in impact structures and contribute to a broader understanding of the complex physical processes that operate in zircon during the impact cratering process.

Key words: zircon, reidite, shock metamorphism, impact metamorphism, phase transition, microtexture, microstructural evolution, solid-state recrystallization, high pressure temperature, electron backscatter diffraction (EBSD), Raman spectroscopy

Classification system and/or index terms (if any)

Supplementary bibliographical information — **Language:** English

ISSN and key title: 1651-6648 LITHOLUND THESES — **ISBN:** 978-91-87847-88-2 (print) **ISBN:** 978-91-87847-89-9 (pdf)

Recipient's notes — **Number of pages:** 170 — Price

Security classification

Signature Date: May 16, 2025

When the pressure builds up, don’t break—transform.

– *Ancient proverb from a random zircon crystal*

Table of Contents

List of papers

This thesis is based on the three papers listed below, which have been appended to the thesis. Paper I is reprinted under permission of John Wiley and Sons (Wiley-Blackwell publishing). Paper II is published here under the permission of and Mineralogical Society of America (if the manuscript is accepted by the journal). Paper III is a manuscript to be submitted.

Paper I

Anders Plan, Gavin G. Kenny, Timmons M. Erickson, Paula Lindgren, Carl Alwmark, Sanna Holm-Alwmark, Philippe Lambert, Anders Scherstén, Ulf Söderlund. (2021), *Exceptional preservation of reidite in the Rochechouart impact structure, France: New insights into shock deformation and phase transition of zircon.* Meteoritics & Planetary Science, *56*:1795–1828.

Paper II

Anders Plan, Sanna Alwmark, Ryan S. Jakubek, William R. Hyde, Aaron J. Cavosie, Timmons M. Erickson. (submitted manuscript, March 2025), *On the Raman spectra of shock metamorphosed zircon – spectral characterization, challenges, and recommended practice.* American Mineralogist.

Paper III

Anders Plan, Timmons M. Erickson, William Hyde, Sanna Alwmark, Roy Christoffersen, Brittany Cymes. (Manuscript), *Shock-induced zircon recrystallization mediated by shear localization.*

Acknowledgments

First and foremost, I want to express my deepest gratitude to Ulf. Having you as my supervisor has been an absolute privilege. Your positive approach, guidance, enthusiasm, and encouragement throughout this journey have made all the difference. I am incredibly thankful not only for your insights and expertise but also for the way you have made this process enjoyable.

Sanna, I sincerely appreciate your support over these years, you really excel as a mentor. Your hospitability, dedication, generosity, and scientific passion have been an incredible source of inspiration. I feel truly lucky to have had someone as brilliant and supportive as you alongside me throughout this project. Your ability to navigate even the most challenging obstacles with clarity and patience has been invaluable, and I deeply appreciate your encouragement and guidance every step of the way.

I am highly grateful to my co-supervisor, Timmons. Your expertise and fresh perspectives have been instrumental in shaping this work. Thank you for your invaluable feedback, your willingness to answer questions, and for always providing thoughtful insights over the projects have really strengthened this research.

Paula, thank you for introducing me into the scientific field of impact cratering, impact metamorphism, and electron backscatter diffraction analysis. You have been a fantastic and kind co-supervisor, and I am grateful for your time, effort, and thoughtful input throughout my Ph.D.

A huge thank you to the planetary research group (both old and new members) for fostering an environment that has been both stimulating, welcoming and fun. The discussions, collaborations, and shared experiences have made this journey more rewarding. Special thanks to Will, Carl, Gabriel, Josse, Patrycja, Katarzyna, and Leif for the engaging conversations, great teamwork, and for making the workplace a fun and inspiring space.

To my fellow PhD students, past and present, I am grateful for the camaraderie, support, and good memories. Big thanks to Will, Miguel, Gabriel, Niklas for all the good times and jokes! I have been fortunate to share an office with amazing colleagues: Gabriel, and Julia—thanks for the good laughs and keeping the plants alive.

I also want to extend my gratitude to those who have contributed to the analytical work in the various projects. Big thanks to Roy Christoffersen and Brittany Cymes, at NASA, for offering their dedication and technical skills to actualize the TEM-work. Milda Pucetaite, at Lund University, thank you for setting up the Raman instrument and showing me the operation procedures.

To my co-authors, thank you for your patience, collaboration, fruitful discussions, and valuable feedback. I appreciate your constructive comments and for responding to my e-mails with patience and efficiency.

Lastly, to the most important people in my life, mamma, pappa, Marie, Emelie, Tomas, to my love Linn (the most amazing soul out there), the most excellent cat Sonic (a welcome distraction in time of need), thank you for always being there, for your unwavering support, and your curiosity (e.g. in dödisgropar). I could not have done this without you. To my late grandmother Gunborg (miss you), which initially sparked my interest in geology during my childhood. A big heartfelt thanks to my childhood friends Stefan, Erik, and Anders—in a situation such as this I would like to say: Givet jobb! Heda tôrk full!

Parts of my grandmother`s rock collection, sampled from various localities around Scandinavia during her journeys.

Basic definitions and abbreviations

Here are definitions and abbreviations of the most important terms used in this thesis.

FRIGN zircon:	(Former Reidite in Granular Neoblastic zircon), a microstructural texture in zircon that forms through the recrystallization of its high-pressure polymorph, reidite, during post-shock temperature excursion. These grains are characterized by a granular neoblastic appearance, FRIGN zircon retains systematic crystallographic orientations inherited from its precursor phase, reidite, thus serves as thermobarometric record of both high-pressure conditions and extreme, subsequent high-temperature.
Hypervelocity (collision):	Typically exceeding 5 km/ s^{-1}, characteristic of collisions between planetary bodies. At these speeds, the energy released upon impact is sufficient to produce extreme pressures and temperatures, leading to impact metamorphism and the formation of impact structures.
Impact cratering/event:	The process by which a high-velocity collision between planetary bodies generates a crater, accompanied by extreme pressures and temperatures that induce shock metamorphism in the target rocks.
Impact metamorphism:	This thesis diverges from the classic impact nomenclature, and the use of shock metamorphism. This term comes from Stöffler and Grieve (2007): "*The material engulfed by the shock wave is affected by what is collectively called impact metamorphism. Impact metamorphism should be applied only for natural rocks and minerals, and it includes solid state deformation, melting and vaporisation of the target rock(s) and their constituents minerals. The term shock metamorphism is a more general term that can be used irrespective of the process which generates a shock wave: Natural impacts or artificial hypervelocity impacts or explosions of chemical or nuclear explosive devices*".
Impact structure:	A geological feature formed by the collision of planetary bodies at or near cosmic velocities, resulting in the formation of a crater and the development of diagnostic shock metamorphic features within the target rocks. In many cases on Earth, the original crater morphology has been significantly modified or obliterated by post-impact processes such as erosion, sedimentation, or tectonic deformation.
Phase transformation:	A permanent structural change in minerals, converting from one phase to another, triggered by variations in pressure-temperature. During impact cratering, phase transformations occur under extreme P-T conditions, and can produce high-pressure polymorphs—such as the conversion of zircon to reidite.
Reidite:	The high-pressure polymorph of zircon.
Shock metamorphism:	Permanent deformation in minerals and rocks subjected to hypervelocity impacts.
BSE:	Backscattered Electron
CL:	Cathodoluminescence
EBSD:	Electron Backscatter Diffraction
EDS:	Energy Dispersive Spectroscopy
SEM:	Scanning Electron Microscopy
TEM:	Transmission Electron Microscopy

1 Introduction

Impact cratering – a vital cosmic process

Besides the eight planets in the Solar System, countless asteroids and comets orbit the Sun. These objects are remnants of the proto-solar nebula and relics of planetesimals, dating back to the formation of the Solar System approximately 4.6 billion years ago. Throughout deep time, collisions between celestial bodies have been a recurring cosmic phenomenon, continuously shaping and reshaping Earth and our celestial neighbors. Impact cratering refers to hypervelocity (>5 km s^{-1}) collisions between solid bodies, a process once considered rare and exotic. However, mankind's space exploration has revealed that impact craters are abundant on every solid planetary surface (Fig. 1). As a result, extensive research has been dedicated to understanding these processes. Today, the scientific community recognizes impact cratering as a fundamental geological process that recurs throughout the solar system and is recognized to be crucial for the dynamical evolution of planets and their satellites.

From a planetary perspective, impact cratering and the thermal evolution of impact structures are considered a major contributor to the emergence of life and to have played a casual role for planetary habitability. Both asteroids and comets are capable of harboring essential building blocks of life, such as ammonia, methanol, and glycine—the chemical precursors to amino acids (Glavin et al., 2025). These components are critical components for constructing DNA and RNA molecular chains (e.g. Callahan et al., 2011). Additionally, studies have demonstrated that complex organic compounds can be synthesized through impact events (e.g. Bar-Nun et al., 1970, Furukawa et al., 2015, Takeuchi et al., 2020), which offers explanations for the detection of amino acids detected in meteorites (e.g. Cobb and Pudritz, 2014, Koga and Naraoka, 2017, Chan et al., 2018). These findings have led to the hypothesis that these extraterrestrial objects may have served as a primary source of the chemical evolution necessary for the origin of life on Earth and potentially beyond—a concept known as "panspermia" or "cosmic seeding" (e.g. Line, 2007).

During early Earth's history, impact sites may have provided ideal habitats for primitive microorganisms. In the absence of a developed atmosphere, impact-generated fractures and micropores in rocky substrates could have offered protection from intense ultraviolet radiation, while impact-induced hydrothermal systems acted as an energy source and provided a continual influx of water and essential nutrients (e.g. Abramov and Mojzsis, 2009, Pontefract et al., 2014). These conditions may have facilitated the survival and development of early life in the otherwise harsh and inhospitable environment (e.g. Osinski et al., 2013). As a result, impact craters are prime targets for extraterrestrial life-detection missions, particularly on Mars, where ancient impact-induced hydrothermal systems may have supported past microbial life. In order to understand Earth's geological and biological evolution over deep time, impact events must be taken into consideration. The aftermath of large impacts has the potential to generate catastrophic consequences with dramatic alteration to the climate, atmospheric composition, and oceanic chemistry (e.g. French 1998). One of the most well-known examples is the Chicxulub impact, a 180 km-wide crater on the Yucatán Peninsula that formed approximately 66 million years ago (Alvarez et al., 1980). This event has been correlated to cataclysmic environmental changes that ultimately lead to the Cretaceous-Paleogene (K-Pg) mass extinction. In the aftermath, approximately 75% of Earth's species were wiped out, including non-avian dinosaurs (Alvarez et al., 1980). Thus, impact-induced catastrophes have profoundly shaped biological evolution by influencing which species survived and thrived in the aftermath. The link between impact events and mass extinctions highlights the importance of understanding these processes and their occurrences over deep time, and the broader implications for the biosphere. However, establishing precise cause-and-effect relationships remains challenging. The terrestrial impact record is inherently incomplete due to erosion, burial, and tectonic activity, which have continuously modified, buried, and erased impact structures over geological time, respectively (Osinski et al., 2022). While over 200 impact craters have been identified on Earth, these structures likely represent only a fraction of all that have occurred throughout geological history (Schmieder and Kring, 2020). In contrast, planetary bodies with limited geological activity (Fig. 1a–1c), such as the Moon and Mars, host over 100,000 and 380,000 craters (>1 km in diameter), respectively (Robbins and Hynek, 2012, Yang et al., 2020). The sheer number of recognized craters underscores the

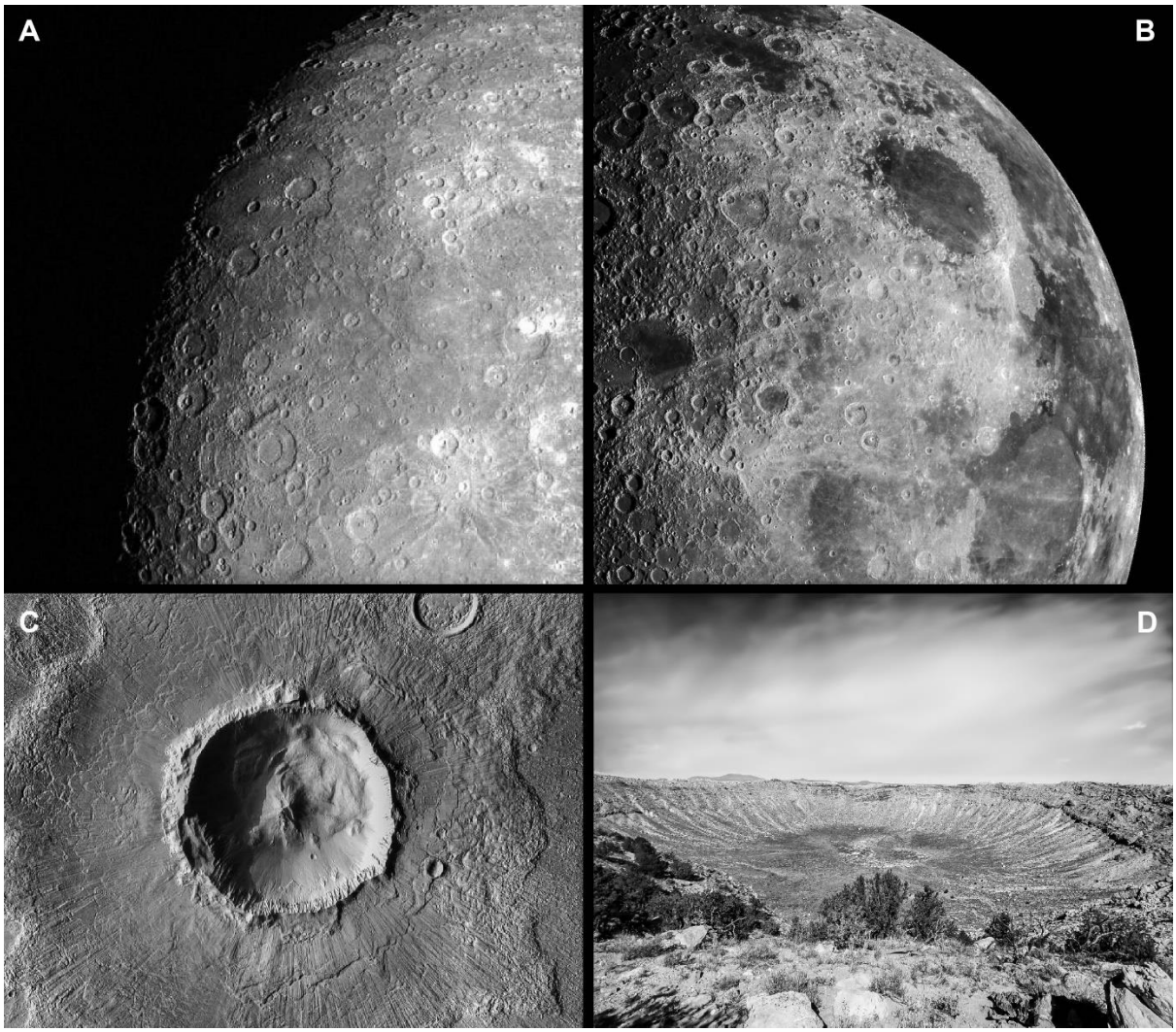

Figure 1. Examples of various impact craters in the Solar System. A) Impact crater mosaic on the surface of Mercury. B) Orbital image over the north nole of the Moon, exhibiting impact craters of different sizes. C) Image from the NASA Mars Odyssey spacecraft of the 20.8 km wide Bacolor Crater situated on the Utopia Planitia, Mars. The crater is classified as complex and has a series of well-preserved features, a central uplift encompassed by crater terraces and walls. Surrounding the crater is secondary craters within a layered ejecta deposit that formed during a surge of superheated gas and ballistically ejected debris. D) Photograph overlooking the 50,000 years old, and 1.2 km wide Meteor Crater located in the desert of northern Arizona (U.S.), known to be one of the best-preserved impact craters on Earth (Photograph credit Fig. 1a–1c: NASA/JPL-Caltech/ASU, Fig. 1d: the authors photograph from field work).

significance of impact cratering as one of the most prominent and persistent surface-modifying processes in the inner solar system (Chyba, 1990, O'Neill et al., 2017, Erickson et al., 2020). Given the fragmentary nature of Earth's impact record, further discoveries will provide additional valuable insights into the role of impact cratering for planetary and biospheric evolution. Beyond Earth, continued exploration of impact structures on other planetary bodies continues to enhance our understanding of crater formation processes and their implications for planetary history (e.g. Shkolyar et al., 2022).

Impact cratering remains one of the most significant yet incompletely understood processes in planetary science. While substantial progress has been made in identifying craters, dating impact events, and reconstructing their effects (see e.g., reviews in Osinski and Pierazzo, 2013). Many fundamental questions still remain: How has Earth's impact flux varied over geological time? How do impact-induced hydrothermal systems contribute to prebiotic chemistry and the potential emergence of life? To answer such questions, a multidisciplinary approach is required. Sample-return missions, such as those conducted by the Hayabusa2 spacecraft (e.g. Yada et al., 2022) and the upcoming Mars sample-return mission (e.g. Sarli et al., 2024), promise to provide direct access to impact-modified materials. New discoveries will further illuminate the role of impact cratering in shaping Earth's and other planetary bodies'—further reinforcing impact cratering as an important process to understand planetary history.

In recent decades, zircon has emerged as a crucial mineral in the study of impact cratering. The mineral can preserve various impact metamorphic features related to the extreme pressure–temperature conditions generated during impact events which has resulted in calibration of impact-generated thermobarometric parameters. These various shock-induced features, combined with zircon's ability to retain radiogenic isotopes utilized for U–Pb dating, make it a powerful tool for both identifying and put absolute age constraints on impact events. However, despite its widespread use, important questions remain—particularly regarding zircon's response and stability under different pressure–temperature regimes, and the thresholds at which specific microstructures form. This thesis aims to address these enigmatic issues and provide deeper insight into the deformation mechanisms that govern the behavior of zircon under the extreme environments associated with hypervelocity impact events.

2 Impact cratering process – the fundamentals

2.1 Contact and compression stage

When an impactor collides with a planetary surface at hypervelocity, the contact and compression stage is initiated (Fig. 2a). This is the first and most violent phase of impact crater formation. This process transpires during seconds, but the energy release is capable of generating extreme pressures and temperatures that permanently alter the target material. Upon collision, the projectile penetrates the crust to a depth corresponding to ≤2 times the projectile diameter (Kieffer and Simonds, 1980). The kinetic energy of the projectile is instantaneously converted into shock waves that propagate outward in a hemispherical pattern and are transmitted through both the impactor and the target rock (Fig. 2a) (Melosh, 1989). The passages of shock waves cause swift compression of the target material with the capability to generate pressures gradients that exceed 100 GPa—far greater than those achieved in any terrestrial tectonothermal process (<3 GPa) (Melosh, 1989). In rapid progression, the shock waves interact with targeted materials and are reflected towards the direction of the impactor. The shock wave that enters the impactor is transmitted until it reaches the back of the body and is reflected back as a rarefaction (release) wave (Fig. 2a). The sudden decompression causes the projectile to instantaneously fragment, melt, or vaporize completely, depending on its composition (Osinski and Pierazzo, 2013). Stony or icy impactors are more likely to undergo vaporization, whereas metallic (e.g. iron) impactors may survive in molten form and mix with the target material. As a result, impactor fragments may be preserved in impactites and/or ejected into the atmosphere, and/or even space as part of the vapor plume (Melosh, 1989). The overall conversion of mechanical work into heat leads to extreme but transient temperature conditions at the impact site, further promoting various deformations of minerals. The immense heat generated during this phase also leads to the formation of impact melt sheets, which may line the crater floor or be ejected. One of the most defining processes of this stage is impact metamorphism, a set of irreversible mineralogical deformations caused by the extreme pressure and temperature conditions during the compression-decompression and post-shock heating (further discussed in chapter 3 and 4). As the shock wave continue to travel outward, the waves successively lose energy due to heating, deformation, and acceleration of target rocks. Due to the overall energy loss, the shock waves transitions into seismic waves (Melosh, 1989). The process then starts to shift towards the excavation stage, during which the transient crater forms and expands, and large volumes of material are ejected outward from the impact site.

2.2 Excavation stage

The excavation stage follows immediately after the intense compression of the contact stage. This stage is driven by the expansion of shock waves through the target material, which displaces rock and generates excavation flows as an outcome (Fig. 2b). The process occurs within seconds to a few minutes, depending on the energy release (at this stage, the impactor is completely melted/vaporized) and the size of the impact which and results in the formation of a transient crater (Fig. 2b, red color). This temporary cavity represents the maximum extent of material displacement before gravitational forces modify the structure (Fig. 2b) (Melosh, 1989). The excavation phase is fundamental to determining the overall morphology of the final crater and further dictates the

distribution extent of ejected material and likewise the (re-)arrangement of impact substrate. During this stage (Fig. 2b), the highly energetic shock waves propagate through the target material. The imposing shock stress-strain field and the ensuing unloading (i.e. release wave) far exceed the mechanical strength of rocks, thus causing fracturing, fragmentation, brecciation, cataclasis, pulverization, and melting of rocks (Melosh, 1989). The imposed energy generates an "explosion" that produces a transient cavity with a bowl-like shape wherein shocked materials are ejected upwards and outwards, and become displaced downwards (Fig. 2b, dashed arrows). As a result, two primary zones are generated: (i) the excavated zone and (ii) the displaced zone (Fig. 2b).

(i) Outwards from the crater wall and the crater rim, debris are ballistically discharged and forms a thin ejecta blanket around and away from the depression (Fig. 1c, 2c) (Melosh, 1989). Impact ejecta deposits consist of a rich admixture of mostly melt and highly shocked materials which can represent prominent crater features with great lateral extent (Glass and Simonson, 2012). The proximal ejecta material may continuously extend several crater diameters away from the impact site, with the largest fragments deposited near the crater rim and finer particles traveling much farther. On planetary bodies that lacks or have a thinner atmosphere (relative to Earth), such as Mercury, the Moon, and Mars (Fig. 1a–1c, respectively), ejecta blankets may be well-preserved features. Secondary craters are often observed in these ejecta deposits. These smaller craters are generated by high-velocity fragments that re-impacted the surface (Fig. 1c). However, on Earth, atmospheric resistance can alter the ejecta distribution, and ensuing erosion may erase these features over time. Ejecta deposits are classified according to their proximity to the crater. A distal impact ejecta is defined if deposition occurs >2.5 crater radii from the crater rim—having the potential to be distributed around the entire planetary surface (Glass and Simonson, 2012). Whilst a proximal impact ejecta defines deposition <2.5 crater radii from the rim. As the excavation progresses, a vapor plume also develops above the impact site, which comprises vaporized and fine-grained fragmented target material (Melosh, 1989). The vaporized and molten components of the impact plume can also condense into small spherules and glassy particles during atmospheric flight and can settle over vast areas—serving as key stratigraphic markers (i.e. tektite strewn field) (Stöffler, 1984, Simonson and Glass, 2004). To date, 46 impact (ejecta) deposits have been confirmed and represent the only preserved evidence of hypervelocity collisions in the Archean records (dating back to 3,470 Ma, the source crater for a majority of these deposits remains unknown) (Glass and Simonson, 2012), thus outdating the oldest impact structure confirmed on Earth, the Yarrabubba (i.e. 2,229 Ma) (Schmieder and Kring, 2020).

(ii) In contrast, the displaced zone comprises material that is forced downward and outward within the crater but lacks the kinetic energy necessary for ejection (Fig. 2b). This material is structurally and variably deformed, often forming complex lithological arrangements of fractured and brecciated rocks (i.e. impactites, further discussed in chapter 3), which eventually settles and becomes preserved within the final structure. Towards the end of the excavation stage, the central regions of complex craters undergo adjustments during uplifting—initiating the formation of the central uplift (Fig. 2c). The formation of the transient crater represents the culmination of the excavation process, where the size and depth of the final structure is dictated by the energy release from the impactor and the properties of the target material. In simple craters, the transient cavity closely resembles the final impact structure (Fig. 2b, 2c). However, in larger events, gravitational collapse significantly modifies the final crater shape. The last structural adjustment into a more stable form occurs during the final cratering stage: the modification stage.

2.3 Modification stage

The modification stage represents the final stage of impact crater formation, during which the transient crater undergoes structural and morphological transformations primarily governed by gravitational forces (Fig. 2d). This stage begins immediately after the excavation stage and can span over minutes (e.g. collapse under gravity) to millions of years (e.g. post-impact hydrothermal system; not discussed in this thesis). The extent of modification can vary significantly depending on crater size and the physical properties of the target material (Melosh, 1989). Collectively, these factors ultimately determine whether the final crater retains a simple, bowl-like shape or if it evolves into a more complex structure with central peaks, terraced crater walls, and peak-ring formations (Kenkmann et al., 2014). Smaller impact craters on Earth, typically less than 2–4 km in diameter, only undergo limited modification and therefore are classified as simple craters (Fig. 2) (Melosh, 1989). Their final morphology remains largely similar to the transient cavity (discussed in chapter 2.2), with only minor adjustments such as

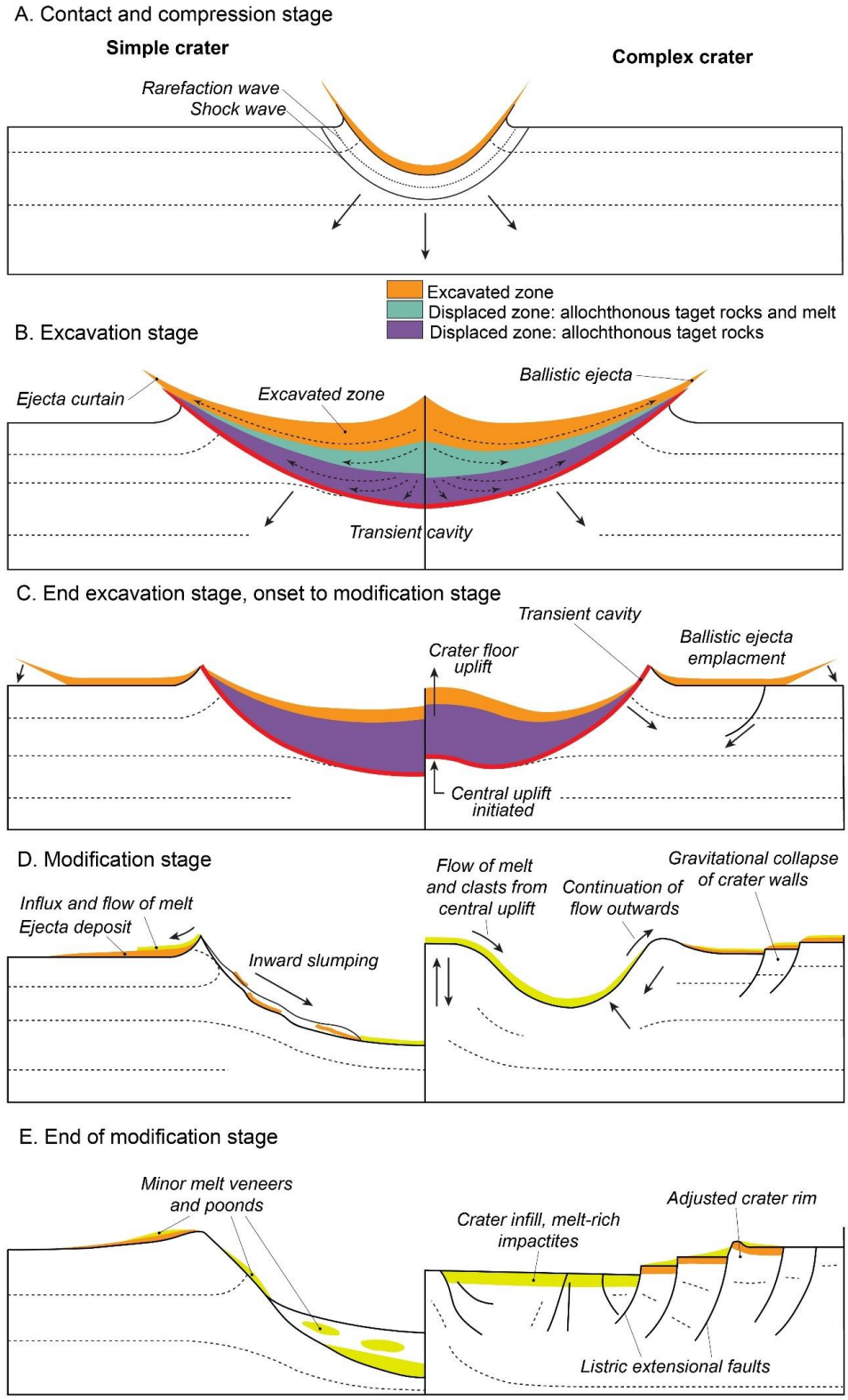

Figure 2. Schematic cross-section illustrating the stages of hypervelocity impact crater formation in a non-marine target. The left side represents the formation of a simple crater, while the right side depicts the development of a complex crater. A) Contact and compression stage: shock and rarefaction waves propagate through the target material. The excavated zone is here generated. B–C) Excavation stage: material displacement within and outside the crater. The formation of the transient cavity (red color) takes place during (B). In complex craters, the transient cavity undergoes rebound at the central regions, the onset of central uplift marks the transition to the modification stage. D–E) Modification stage: In simple craters, debris slumps inward, while in complex craters, gravitational collapse and uplift governs the shape of the final structure morphology. (E) Final crater morphology with terraces, adjusted crater rim, and melt-rich impactites deposits. Figure modified after Osinski and Pierazzo (2013)

inward slumping of crater walls and deposition of ejecta (Fig. 2d). The final crater deposit will consist of rock debris mix with melt (Fig. 2e) (Stöffler, 1971). In contrast, larger impacts produce transient craters that are highly structurally unstable, leading to significant post-excavation modifications (Fig. 2d). These structures are classified as complex craters, and are defined as such, if the structure exceeds 4 km in diameter on Earth (Fig. 2). However, this classification is dependent on the internal strength of the target rock. Sedimentary units may form complex craters <4km, whilst the diameter for crystalline targets is regarded to ≥4 km (Melosh, 1989). The structural adjustments generally modify the initial precipitous crater walls of the transient cavity by a collapse inward along concentric faults, forming a series of terraces around the crater rim (Fig. 2d). Simultaneously, the central region of the crater undergoes uplift due to the elastic rebound of deeply buried target material—forming a prominent central peak (Fig. 2c–2d). As the entire central uplift area undergoes rapid exhumation of deep-seated rocks, otherwise inaccessible material is delivered to the surface and becomes admixed with the material flow from the central peak slope (Fig. 2c–2d) (Melosh, 1989, Osinski and Pierazzo, 2013). The gravitational collapse of the crater walls generates a series of listric extensional faults proximal to the adjusted crater rim (Fig. 2d–2e). The final crater fill will be comprised of impactites rich in melt (Fig. 2d–2e). For even larger impact events, particularly those exceeding ~50 km in diameter, crater modification processes become increasingly complex. A peak-ring basin is such an example. These structures are characterized by an annular concentric ring that emanates from uplifted material and encompasses the central depression completely. Such morphological expressions are regarded to be generated by the collapse of an initially over-steepened central peak (Kenkmann et al., 2014). There are even further observations of more extreme structures of highly complex morphological features—multiring basins. Thes impact structure consists of multiple concentric rings which reflect the occurrence of large-scale gravitational adjustments within the crater. The exact mechanisms behind these multi-ring basins remains a conundrum, though research suggests that the process to generate such structure might be related to deep crustal deformation and fluidized rock movement in response to an immensely large impact event (Melosh, 1989).

While the initial stage of crater modification occurs rapidly, longer-term geological processes continue to reshape the structure over extended timescales. On Earth, rejuvenation of the crust, sedimentation, erosion, and post-shock induced hydrothermal alteration contributes to the progressive degradation of impact craters, often obscuring their original morphology or obliterating these surface scares entirely. The modification stage thus represents a dynamic and ongoing stage of impact cratering. The three impact stages are closely linked to the shock deformation that both rocks and minerals are subjected to, some of which are unique products of impact metamorphism that can provides crucial evidence and insight to impact cratering processes.

3 Impactites

Throughout the three impact cratering stages, target rocks are compressed, decompressed, and heated under extreme P–T conditions (Stöffler, 1971, French, 1998). These conditions are however transient but produce distinct impact metamorphosed lithologies collectively denoted as impactites. Impactites includes various types of different units, for example, suevitic breccias, and impact-melt rock (Stöffler, 1971, Stöffler et al., 2018) (Fig. 3). For complex craters, the final infill comprises emplacement of impactites often found in a specific sequence: the crater floor defines the depth extent of the crater and, in following order, is superimposed by lithic breccia → “melt-poor” suevitic breccia → “melt-rich” suevitic breccia → impact melt rock (cf. Fig. 3). Fine-grained deposits (e.g. fall-back ejecta, impactoclastite, and/or resurge debris in the presence of water) can be intercalated within the top units (Fig. 3b), however preservation of such layers is rare due to post-impact erosion processes. The stratigraphic sequence are products of the various processes directly related to the three aforementioned impact stages (Fig. 2).

The distribution of impactites within and around an impact crater is closely linked to the excavation and modification stages of crater formation (Fig. 2). Autochthonous impactites define constituent materials that have largely remained immobile with minimal displacement from the original location (Fig. 3a). These impactites typically comprise fractured rocks to cataclastic (monomict) breccias situated at the crater rim or anchored to the crater floor (Melosh, 1989). In contrast, parautochthonous impactites constitute displaced material that retain some degree of structural

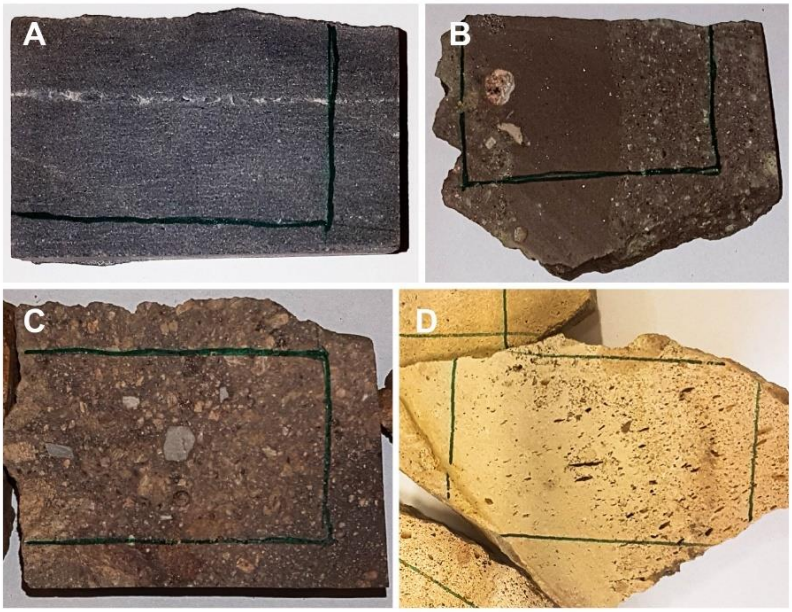

Figure 3. Examples of various impact lithologies from the Rochechouart impact structure. A) Gneissic target rock anchored to the crater floor; minor shock features occur (e.g. shatter cones, Fig. 4a). B) Impactoclastite is interpreted as fine grained fallback ejecta. C) Polymict suevitic breccia. D) Impact-melt rock, note the elongated vesicles preferentially aligned with the flow direction. Green line markings on the samples are for manufacturing thin sections.

coherence but often appear as disrupted target rocks within the crater (Melosh, 1989). Allochthonous impactites represent transported material either within or beyond the impact structure and are further categorized as proximal or distal depending on their final position (Fig. 3b–3d). Proximal allochthonous impactites include (polymict) suevitic breccias (Fig. 3c), and impact melt rocks (Fig. 3d), which are typically found within or immediately in the vicinity surrounding the crater. Suevitic breccias, consist of fragmented target material cemented together with melt components and, generally, account for the most common types of impactites (Fig. 3c). These breccias can either be clast-rich or matrix-dominated, depending on the relative proportions of solid fragments to fine-grained material. In complex craters, suevitic breccias often form when molten rock mixes with lithic clasts, creating a heterogeneous lithology. In some cases, extensive impact melt sheets can form, particularly in craters produced in crystalline target rocks, where high shock pressures generate significant melting (Fig. 3d). These melt sheets can later solidify into coherent rock formations, often exhibiting vesicular flow texture (Fig. 3d) and generally have undergone rapid cooling, hence glass-bearing (Stöffler, 1984). As previously discussed, distal impactites, including tektites and spherules, and may be displaced hundreds to thousands of kilometers from the source crater (Glass and Simonson, 2012). The transport and deposition of ejecta create additional forms of impactites, including layered ejecta blankets and airborne spherules (as discussed in chapter 2.2).

Despite the chaotic formation of impactites, these rocks serve as crucial geological markers for recognizing and studying impact structures. Their unique characteristics, particularly in melt-bearing and brecciated forms, can aid in distinguishing them from volcanic or tectonically altered rocks, but evidence of the impact cratering process needs to be further constrained in order to perform proper classification (Stöffler, 1971, Stöffler et al., 2018). Through continued research, impactites and their hosted shock materials and minerals have provided diagnostic evidence of impact events. The understanding and the study of impact metamorphic effects in both rock forming minerals and accessory minerals have increased our understanding into the dynamic process of impact events (e.g. Stöffler, 1972). Thus, understanding the response of various minerals over a wide range of shock conditions allows reconstruction of the tectonothermal history of the impact process, and characterization of various impact-induced deformation features in minerals have provided diagnostic evidence of impact cratering and impact metamorphism.

4 Impact metamorphism

With the development and easy accessibility of high-resolution satellite imagery, geophysical data (e.g. gravimetry), and especially insight into the shock effects, the terrestrial impact record has steadily grown over the decades. On the basis of circular morphologies alone, suggestions regarding newly proposed impact structures can been disputed as such formations can also be products of common conventional geological processes (e.g. tectonic

deformation, volcanism, diaperism, salt-domes etc.). Some proposals can be considered as vastly speculative (e.g. Rocca et al., 2017, Sieh et al., 2020), as substantial evidence for an impact origin is either poorly constrained or non-existent. Confirmation of structures as products of impact cratering requires the discovery of preserved diagnostic evidence that are directly linked to the impactor or the extreme impact-induced P-T conditions. Currently, these fingerprints include: (i) preserved fragments of the meteorite, (ii) remnant geochemical signatures from the impactor (e.g. iridium and PGEs anomalies), and (iii) shock-metamorphic effects (e.g. shatter cones, high P/T glass and mineral polymorphs, and various shock metamorphic deformation features in minerals such as PDF in quartz; Fig. 4a, 4b) (Koeberl, 2002, French and Koeberl, 2010).

Impact metamorphism refers to the suite of irreversible physical and chemical modifications which occur in minerals when subjected to the extreme pressures and temperatures generated during hypervelocity impact events (far above the Hugoniot elastic limit) (Stöffler, 1972, Melosh, 1989, Langenhorst and Deutsch, 2012). These conditions far exceed P-T of common endogenic geological processes (Fig. 4). The generated shock waves propagate through target materials at supersonic speeds and impose high stress fields (Kenkmann et al., 2014, Rae et al., 2021). Therefore, the resulting deformation is highly contrastive to what tectonothermal processes yields (conventional metamorphism occurs over long timescales, under static P-T conditions, whilst impact metamorphism transpires almost instantaneously). Thus, the mineralogical effects of impact metamorphism are unique in nature and can be utilized for identification and characterization of impact cratering processes and calibrations of P-T(-t) conditions (Stöffler, 1972, French and Koeberl, 2010). The passage of a shock wave through target rocks initiates a complex sequence of deformation processes, with pressure and temperature increasing rapidly before dissipating swiftly. The initial shock pressures can exceed 100 GPa at the point of impact and gradually decrease outward, forming concentric shock zones (Melosh, 1989). The magnitude of these pressures-temperature gradients determines the nature of the shock metamorphic imprints (e.g. Stöffler, 1972, Grieve et al., 1996). In the low-pressure regime (~2–10 GPa), macroscopic deformation features such as shatter cones form (Fig. 4b)—providing a diagnostic indicator of an impact event. Shatter cones appear as striated, conical fractures that develop in fine- and medium-grained lithologies, and their formation is attributed to the intricate interplay of shock (e.g. compressive and rarefaction) waves within the rock (Osinski and Ferrière, 2016). Alongside shatter cones, minerals begin to exhibit microscopic deformation features, commonly including kink bands, various planar fractures/features and mechanical twinning (Stöffler, 1972, French and Koeberl, 2010). Quartz (SiO_2) has historically been the hallmark mineral of the study of impact metamorphism (Melosh, 1989, and the references therein). The section below, mainly, describes common impact metamorphic deformation features in quartz meant to serve as an example, of which only a few characteristic examples are stated here.

As shock pressures increase beyond ~10 GPa, thus surpassing the Hugoniot elastic limit (HEL) of quartz, more profound structural changes occur. At these conditions, distinctive shock-induced transformations occur which serve as reliable thermobarometrical recorder of impact conditions (e.g. Holm-Alwmark et al., 2017). In the 10–35 GPa range (e.g. Stöffler et al., 2018), quartz develops planar deformation features (PDFs, Fig. 4a), which appear as sets of parallel and closely spaced lamellae. The PDFs form due to the reorganization of the crystal lattice in response to rapid shock compression, and their orientation corresponds to different pressure regimes—making it possible to calibrate the intensity of the impact event (e.g. Holm et al., 2011). At these shock conditions, quartz can also undergo phase transitions into various high-pressure polymorphs such as coesite (~10–15 GPa) and stishovite (~12–30 GPa) (e.g. Hemley, 1987, Melosh, 1989). These polymorphs form when the shock wave readjust silicon–oxygen bonds thus creating a more densely packed crystal structure. Apart from quartz, various high P-T polymorphs of other phases represent a mineralogical fingerprint that can serve as links to impact cratering processes and proxies to specific P-T conditions (e.g. French and Koeberl, 2010). At even higher pressures (~30–45 GPa), the shock waves are capable of imparting sufficient energy to disrupt translation symmetry of the quartz crystal lattice without inducing melting. This results in the formation of diaplectic glasses (e.g. Stöffler, 1984). Unlike conventional volcanic glasses, which form through melting and subsequent quenching, diaplectic glasses are produced by the direct collapse of the atomic framework due to the extreme shock compression and decompression (Stöffler, 1984). In both quartz and feldspar, this process leads to the development of optically isotropic diaplectic glass whilst the original grain morphology is still preserved (e.g. Fritz et al., 2019). With shock pressures of ~50 GPa, the target materials begin to

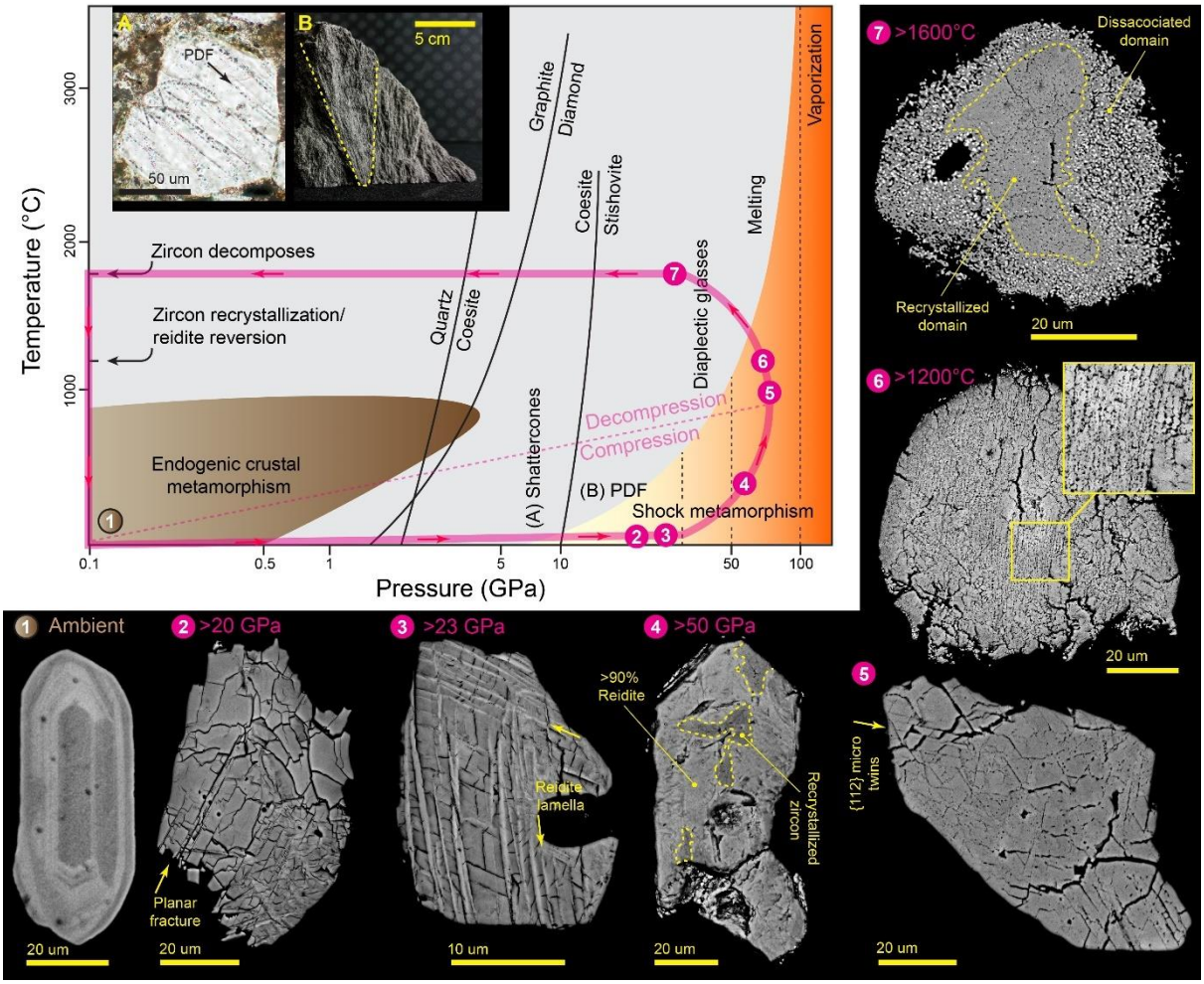

Figure 4. A pressure-temperature diagram illustrating the extreme conditions of impact metamorphism (yellow-red field) with conventional endogenic crustal metamorphic conditions on Earth (brown field). The pressure range for crustal metamorphism reaches up to 3 GPa and temperatures peaks at approximately 1000°C, sufficient to convert graphite into diamond. In contrast, impact metamorphism occurs at pressures exceeding 5 GPa, and can surpass 100 GPa, with temperatures rising above 3000°C. The diagram also illustrates the formation conditions of key shock metamorphic features discussed in the main text, for example: (A) shattercones, (B) planar deformation features in quartz (PDF), and the transition between high-pressure quartz polymorphs such as coesite and stishovite. Note that the x-axis is logarithmic. Modified from French (1998) and Osinski et al. (2022). A schematic P-T pathway for zircon impact metamorphism is outlined in pink color. The pathway highlights the formation of common shock features constrained to specific shock-induced P-T conditions under either compression or post-shock excursion (decompression back to ambient). 1: unshocked zircon (ambient P-T conditions); 2: planar deformation features; 3: reidite lamellae; 4: massive reidite (e.g. domain habit); 5: zircon and reidite {112} micro-twins; 6: reidite to zircon reversion by solid-state recrystallization, forming FRIGN zircon (inset square, note the myriads of zircon neoblasts); 7: zircon dissociation (ZrO_2 + SiO_2). The zircon grains, quartz grains, and shattercones, are part of this thesis work and have undergone EBSD-analysis to constrain the various shock features.

undergo selective melting (Melosh, 1989). The sudden shock release that ensues peak shock compression results in a rapid temperature increase, with localized pockets of molten material forming within the rock matrix. This melting follows a consecutive order. Firstly, mineral phases with lower melting points, such as feldspar, is affected, while relatively more refractory minerals like quartz may persist as diaplectic glass (e.g. Stöffler et al., 2018). Under these high temperatures (>1500°C) refractory accessory minerals, such as zircon, can disassociate into their oxides constitutes (e.g. zircon → ZrO_2 +SiO_2) (Butterman and Foster, 1967, Timms et al., 2017a) (further discussion in coming chapter, 5.2). Overall, the rapid temperature increase results in heterogeneous and complex distribution of various melt phases in the final impactite product.

The distribution of shock metamorphic effects within an impact structure follows a well-defined gradient, with the most intense modifications occurring near the point of impact and with progressively less severe effects extending concentrically outward. This shock zonation can offer crucial insights into the energy dynamics of impact events, allowing for reconstruction of impact events if calibrated correctly (e.g. Holm-Alwmark et al., 2017).

The ability to recognize impact metamorphic features is thus instrumental in both confirming geological structures as being of impact origin and providing insight into the extent of the event. Age determination of impact events is a crucial aspect for reconstruction of geological events. As the mineral zircon can provide both diagnostic evidence of impact cratering and able to provide absolute age constraint for the event, the study of zircon can offer great opportunities for unravelling impact cratering histories (e.g. Krogh et al., 1993, Wittmann et al., 2006, Timms et al., 2017a, Erickson et al., 2020).

5 The mineral zircon

5.1 Chronicles of a significant mineral – the timekeeper of planetary archives

Zircon ($ZrSiO_4$) is regarded as one of the most significant minerals for studying the geological archive due to some remarkable properties. The crystal structure is highly stabile and durable, hence able to retain geochemical and isotopic information over vast time scales (Davis et al., 2003, Hoskin and Schaltegger, 2003). Zircon is a common accessory mineral that occurs in a variety of igneous, metamorphic, and sedimentary rocks (Fig. 4.1). The robust nature of zircon allows it to persist over various harsh processes such as weathering, erosion, metamorphism, and magmatic recycling (e.g. Corfu et al., 2003). Overall, this mineral has a crucial role in our understanding of Earth's history as it has the potential to be utilized as an essential tool for reconstructing past geological events, particularly through U-Pb geochronology (Davis et al., 2003).

The crystal structure of zircon is tetragonal, space group $I4_1/amd$, which consists of isolated SiO_4 tetrahedra that share corners and edges with ZrO_8 dodecahedra (Hazen and Finger, 1979). The presence of channels along the c-axis allows for minor substitutions of elements such as uranium (U), thorium (Th), hafnium (Hf), titanium (Ti), rare earth elements (REE), and phosphorus (P), allowing for a wide range of geochemical applications (Finch and Hanchar, 2003). The incorporation of U and Th, enables zircon to be used for radiometric dating, as these actinides decay over time into stable Pb isotopes (Davis et al., 2003), thus providing a natural clock to determine the crystallization age of the entire crystal (e.g. by isotope dilution-thermal ionization mass spectrometry) or selective domains within the crystal (e.g. secondary ion mass spectrometry). The zircon U-Pb isotopic system is the most widely used method to constrain the geological archive due to the robustness of the U-Pb geochronometer. The two decay chains of uranium—$^{238}U \rightarrow {}^{206}Pb$ and $^{235}U \rightarrow {}^{207}Pb$—have half-lives that are well suited for dating events throughout geological time—from the Hadean to the present (Davis et al., 2003). As zircon incorporates U but excludes Pb during crystallization, the initial Pb content is negligible—favorably for precise age determinations. In geological environments where other geochronometers yield open system behavior, zircon with its structural sturdiness and slow diffusion rate remain as a closed system thus capable of retaining radiogenic Pb over high-temperature conditions. In addition to its role in geochronology, zircon is a valuable recorder of crustal evolution and magmatic processes by analysis the trace element composition. Rare earth elements (REE) are commonly incorporated into zircon via substitution mechanisms, particularly through the coupled substitution ($REE^{3+} + P^{5+} \leftrightarrow Zr^{4+} + Si^{4+}$) (Hoskin and Schaltegger, 2003). The partitioning of REEs in zircon can provide insights into, for example, the composition of the parental magma, crystallization temperatures, and the evolution of magmatic systems in general (e.g. Hoskin and Schaltegger, 2003, Corfu et al., 2003, Hoskin, 2005). Despite zircon's resistant to a wide variety of geological processes, the crystal structure is susceptible to metamictization—a phenomenon caused by the accumulation of radiation damage from the decay of U and Th (Krogh and Davis, 1975, Chakoumakos et al., 1987, Woodhead et al., 1991). Over time, the alpha-decay events continuously displace atoms in the crystal lattice, leading to the breakdown of the zircon structure—hence transitions into an amorphous state. This process results in volume expansion, increased solubility, and potential loss of radiogenic lead, which can severely hamper age determinations. The extent of metamictization can readily be assessed through Raman spectroscopy and be observed by SEM-BSE-CL imagery (e.g. Ming et al., 2000). Both are common methods that can be used to distinguish crystalline, metamict, and annealed domains within zircon grains. The significance of zircon extends beyond terrestrial geology. In planetary science, zircon has been instrumental in studies of the early Earth and extraterrestrial bodies. The oldest known material of Earth consists of Hadean detrital zircon grains from the Jack Hills in Western Australia, with ages exceeding 4.3 Ga (e.g. Valley et al., 2014).

These ancient zircons provide critical insights into the conditions of early Earth, including evidence for liquid water, to Earth's magnetic field, and crustal differentiation (e.g. Mojzsis et al., 2001, Tarduno et al., 2015, Tissot et al., 2019). Zircon has also been identified in lunar and Martian meteorites, offering, for example, constraints on the chronology and thermal evolution of these planetary bodies (e.g. Meyer et al., 1996, Costa et al., 2020). However, in order to utilize zircon for constraining impact events, insights on how zircon responds to the extreme P-T conditions imposed during impact cratering is a necessity (Fig. 4).

5.2 Extreme thermobarometry – between a shock and a hard phase

Exposed to the intense pressures and temperatures generated during impact events, zircon undergoes a range of shock-induced modifications, including plastic deformation, twinning, phase transitions, solid-state recrystallization, and ultimately, dissociation into its oxide constituents (Fig. 4.2–4.7). These transformations occur in a pressure-temperature dependent sequence, were increasing shock intensity will result in progressively more extreme structural changes (Fig. 4) (e.g. Timms et al., 2017a).

At shock pressures <20 GPa, zircon undergoes mechanical deformation which are characterized by irregular fracture networks to micro-cataclastic areas, the development of low-to-high angle boundaries (LABs and HABs), dislocation arrays, and planar deformation bands (PDBs) (e.g. Timms et al., 2012). These features are a result of crystal-plastic deformation (Timms et al., 2017a). At slightly higher pressures (~20 GPa), zircon can develop various crystallographically oriented planar deformation features (Fig. 4.2) (Krogh et al., 1984, Bohor et al., 1993, Kamo and Krogh, 1995, Kamo et al., 1996), analogous with PDFs in quartz but currently lacks crystallographic pressure calibration. The development of these planar arrays indicates an increase in deviatoric stress conditions, where zircon undergoes slip along specific crystallographic planes (Cavosie et al., 2010, Timms et al., 2012, Erickson et al., 2013,).

With increasing shock intensity, at pressure above 23 GPa, zircon undergoes a phase transformation to reidite (Fig. 4.3) (e.g. Szumila et al., 2023), the high-pressure zircon polymorph. Reidite has a tetragonal structure and belongs to the space group $I4_1/a$, having ~10% higher density than zircon (Reid and Ringwood, 1969, Glass and Liu, 2001). However, the transformation mechanism remains a subject of debate. Initially proposed to occur via a displacive, martensitic shear transformation (Kusaba et al., 1985), the zircon–reidite transition has also been interpreted as reconstructive in nature, involving the breaking and reformation of atomic bonds (Marqués et al., 2008). Prior to this thesis, two morphological reidite variants (i.e. habits) have been identified: lamellar and granular habit. Lamellar reidite is characterized by parallel, micrometer- to sub-micrometer-scale bands within relatively crystalline zircon domains, typically formed near peak shock pressures during the passage of a shock wave. Reidite lamellae display a highly systematic crystallographic relationship to the host zircon, with one $\{112\}_{reidite}$ aligning with one $\{100\}_{zircon}$, whilst another $\{112\}_{reidite}$ align with one $\{112\}_{zircon}$, both maintaining an average misorientation of ~5°. Notably, $<110>_{reidite}$ directions are misoriented by ~10° around $[001]_{zircon}$, indicating a consistent but non-coincident interphase relationship. Despite this precise orientation, the habit planes of lamellar reidite show wide variability, often forming along irrational planes, which suggests the transformation is not governed solely by rational lattice matching but may involve rotational accommodation mechanisms (Kusaba et al., 1985, Erickson et al., 2017). The absence of diffusion-controlled features and the presence of sharp misorientation boundaries support a deviatoric shear-dominated transformation (Erickson et al., 2017), rather than dilatational or shuffle mechanisms (Langenhorst and Deutsch, 2012; Delaey, 2006). The formation of lamellae appears largely independent of zircon grain orientation or crystallographic preferred orientation (CPO), instead being controlled by localized structural heterogeneity within the grain (Erickson et al., 2017). In contrast, granular reidite forms in zircon domains of significantly reduced crystallinity, often within metamict areas or along grain boundaries and vugs. These zones are typically CL-dark, indicating substantial radiation damage from accumulated α-decay. In such domains, the zircon lattice has either transitioned to an amorphous state or undergone partial recrystallization, providing the necessary structural conditions for a reconstructive phase transformation (Erickson et al., 2017). Granular reidite grains exhibit topotaxial relationships to their host zircon, displaying subparallel alignment of $<110>_{reidite}$ with both $<110>_{zircon}$ and $<001>_{zircon}$ directions. However, the crystallographic relationship is more relaxed than that observed in lamellar reidite (Erickson et al., 2017, as evidenced by increased angular dispersion in pole figures). This relaxed alignment supports nucleation from an amorphous or diaplectic $ZrSiO_4$ precursor (Erickson et al., 2017),

consistent with *ab initio* simulations of reconstructive transitions under shock conditions (Marqués et al., 2008). In samples from the Ries and Rock Elm impact structures (Cavosie et al., 2015; Erickson et al., 2017), granular reidite is predominantly found at grain boundaries or within vugs, further suggesting that nucleation is favored in structurally compromised zones with a lower state of crystalline. As discussed, the formation of reidite is highly sensitive to the initial structural integrity of the zircon host. Moderately to highly metamict domains inhibit lamellar reidite formation by preventing the propagation of shear due to a lower elastic modulus. Instead, these domains may facilitate granular reidite formation by providing a low-energy pathway for nucleation (Erickson et al., 2017). Combined EBSD and Raman spectroscopy mapping confirms that reidite lamellae preferentially develop in crystalline rims of zircon grains, while metamict cores, despite sometimes exhibiting Raman spectral features suggestive of reidite, lack EBSD evidence of reidite, likely due to either the large volume interaction from the Raman laser or sub-resolution scale of transformation (Erickson et al., 2017). Overall, this highlights the critical role of pre-impact radiation damage in influencing the response of zircon during shock and the ability to preserve high-pressure polymorphs.

At even higher shock pressures, exceeding 40 GPa, the formation of dendritic reidite has been documented (Cavosie et al., 2020). This reidite habit appears to nucleate by rapid quenching during atmospheric flight. While rare in nature, dendritic reidite has been observed in impact ejecta from the Chesapeake Bay impact structure, suggesting that it may represent a unique shock signature of high-energy impact ejected material (Cavosie et al., 2020). Furthermore, constraints from shock and high-P experiments demonstrate that the reidite transformation is complete >50 GPa (Fig. 4.4), as 100% reidite conversion rate has been observed around this pressure gradient (Kusaba et al., 1985, Kusaba et al., 1986, Fiske et al., 1994, Leroux et al., 1999).

At decompression, from minimum 20 GPa, the development of {112} mechanical micro-twins can occur (Fig. 4.5). Unlike growth twins, which form during crystallization processes, shock twins are formed during decompression from impact-induced shear stress and are characterized by a 65° lattice misorientation about a <110> axis (Leroux et al., 1999, Moser et al., 2011, Cox et al., 2018). These twins are frequently hosted within planar deformation features formed on {112} with shear in the <111> direction, suggesting a strong crystallographic linkage for twin formation to specific planes (Erickson et al., 2013).

Upon exposure to temperatures >1,200 °C, reidite undergoes a solid-state reversion back to zircon forming a granular neoblastic microstructure (Fig. 4.6). This process has been observed in both experiments and impact structures (Kusaba et al., 1985, Kusaba et al., 1986, Bohor et al., 1993, Kamo and Krogh, 1995, Wittmann et al., 2006). However, during the reversion, crystallographic imprint of the precursor phase is recorded into the newly formed zircon domains (Cavosie et al., 2017, Cavosie et al., 2016). This phenomenon, termed phase heritage, involves an epitaxial reidite-to-zircon transformation, characterized by systematic crystallographic orientations among the resulting zircon neoblasts, exhibiting high-angle disorientations (~90° ±10°) about the <110> axes conjugating with the [001] direction (Cavosie et al., 2018, Timms et al., 2017a). Such orientation relationships are thus indicative of $ZrSiO_4$ phase transition sequence: zircon → reidite → zircon. A grain with such signature is therefore diagnostic of both high pressures (≥23 GPa) and high post-shock temperatures (≥1200–1673 °C) and are defined as Former Reidite in Granular Neoblastic (FRIGN) zircon (Cavosie et al., 2018).

At temperatures >1,670 °C (Fig. 4.7), zircon becomes thermodynamically unstable and dissociates into its oxide constitutes: ZrO_2 + SiO_2 (Butterman and Foster, 1967, Kusaba et al., 1985, Kaiser et al., 2008). The structural breakdown is common in impact settings where zircon grains are entrained in or adjacent to impact melt. The dissociation initiates with the collapse of the zircon lattice, leading to the formation of a solid ZrO_2 phase—either tetragonal or cubic in structure, depending on temperature—and a coexisting liquid SiO_2 phase that often diffuses into the surrounding melt (Timms et al., 2017a). During post-shock cooling, cubic ZrO_2, stable >2,370 °C, may transition back to the tetragonal form, which eventually transforms into monoclinic ZrO_2, or baddeleyite—the stable polymorph at ambient conditions. These sequential phase transformation pathways can, likewise to FRIGN zircon, preserve crystallographic imprints, enabling reconstruction of the thermal history through phase heritage analysis (Timms et al., 2017b). The identification of baddeleyite as a dissociation product thus signifies complete zircon breakdown and provides a diagnostic signature of post-impact temperatures exceeding the upper zircon stability threshold. These microstructures are crucial in constraining thermal conditions during impact events and serve as a powerful thermobarometric proxy when direct high-

temperature minerals are absent or have reverted (e.g. reidite).

6 Scope of the thesis

The aim of this Ph.D. thesis is to better understand the underlying deformation mechanisms for shock-induced deformation and phase transitions in zircon as this provides critical insight into the pressure-temperature histories of impact events. Zircon, as discussed above, has the ability to record shock features, such as micro-twins, reidite formation, and subsequent reversion (preserved as a crystallographic memory), which makes it a powerful tool for reconstructing impact cratering processes. This thesis focuses toward untangling the complex sequence of various zircon modifications and deformations—from crystal-plastic deformation to polymorphic transitions and dissociation—under a wide range of P-T conditions. These deformations imprints do not only reveal the intensity and duration of shock conditions but can also aid towards decipher impact events in Earth's geological record. To achieve this, state-of-the-art microanalytical techniques, such as Scanning Electron Microscope (SEM), Electron Backscatter Diffraction (EBSD), Transmission Electron Microscopy (TEM), and Raman spectroscopy have been employed. The research objectives are:

I. Provide insights into the underlying deformation mechanisms of $ZrSiO_4$ during impact metamorphism, and to put further constraints to the microstructural evolution related to zircon phase transitioning.

II. Evaluate and refine conventional microanalytical techniques used for characterizing the response and stability of $ZrSiO_4$ subjected to impact metamorphic conditions.

7 Methodologies

7.1 Sample preparation and characterization

Extraction of heavy mineral fractions (e.g. zircon) from a hand specimen follows a stepwise approach. Fresh rock specimens are first crushed with a sledgehammer on a clean steel block, and the rock fragments are grinded to a fine powder using a ring-mill. Water-based gravitational separation (i.e. Wilfley water shaking table) follows in order to extract high density minerals (Fig. 5a)—following the procedures of Söderlund & Johansson (2002). The remaining heavy mineral fraction is suspended in ethanol and magnetic minerals are removed by a handheld neodymium magnet. The zircon grains are thereafter handpicked under a binocular microscope and placed into a petri dish filled with ethanol (Fig. 5a). After the removal of ethanol, the zircon grains are transferred onto a double-sided adhesive tape and encased into standard size (d: 2.54 cm) epoxy-resin mount (Fig. 5b). After hardening, the mount is ready for conventional mechanical grinding and polishing (various diamond paste fractions and grinding-polishing clothes are used) with the aim to expose the mid-section of the grains. Rock slabs from various impactites were also cut out, grinded, and polished (Fig. 5b). For SEM-imaging, the carbon coating was kept to c. 20 nm. The grains are imaged and analyzed by various detectors (i.e. SE-BSE-CL, EDS-EBSD), followed by characterization and cataloguing according to their respective interior microtextures (Fig. 5c).

7.2 Scanning electron microscopy – imagery and crystallographic acquisition

7.2.1 Backscattered electron and cathodoluminescence imagery

Scanning electron microscopy (SEM) is a powerful and essential tool for analyzing geological samples, having the capability to probe the interrogated material with high spatial resolution—down to the nanoscale (Fig. 5d). Among the many capabilities of this instrument, backscattered electron (BSE) imaging

Figure 5. A) Handpicked heavy mineral from the Wilfley extraction. B) Heavy minerals now encased in epoxy resin pucks, and polished rocks slabs. C) Polished epoxy resin pucks exposing the mid-section of the heavy minerals and imaged by SEM-BSE (note the variation in *z*-contrast infer presence of other phases besides zircon). D) The SEM instrument (with BSE-CL-SE-EDS-EBSD detectors) at the Department of Geology (Lund University) use throughout this Ph.D. thesis. E) The TEM-instrument at NASA Johnson Space Center (JSC) (Houston, Texas) used for paper III. F) The investigated FIB-foil that was extracted from a zircon grain studied in paper III (manufactured during analytical work at JSC). G) The Raman instrument at the Department of Ecology (Lund University) used to acquire data for paper II.

and cathodoluminescence (CL) imaging are widely employed for investigating variations in composition, mineral phase distributions, and internal microstructures of minerals.

Backscattered electron imaging in SEM relies on the detection of electrons that are elastically scattered from the sample when bombarded by the primary electron beam (generally operating between 10–25 keV). The intensity of backscattered electrons is strongly dependent on the mean atomic number (*z*) of the target material, as heavier elements backscatter electrons more efficiently than lighter elements. This results in an apparent image contrast where high-*z* mineral phases appear bright (e.g. zircon, monazite) relatively to low-*z* phases which appear darker (e.g. quartz, feldspar) (Fig. 5c). The signal is collected using a solid-state BSE detector which captures variations in backscatter intensity in order to create the final image. The high sensitivity of BSE-imaging to atomic number differences can be utilized to distinguish between various mineral phases (e.g. zircon versus quartz) (Fig. 5c), detecting compositional zoning in minerals (e.g. oscillatory zonation in zircon) (Fig. 4.1), and identifying inclusions (e.g. apatite in zircon), alteration (e.g. metamictization in zircon), and deformation features (e.g. planar deformation features in zircon) (Fig. 4.2). While BSE-imaging is primarily used for atomic contrast, cathodoluminescence (CL) imaging provides complementary information by revealing defects, zoning, and growth histories within minerals. The CL-emission occurs when the primary electron beam (generally operating between 20–25 keV) excites electrons within the sample, causing the release of photons as these electrons return to their ground state. The emitted light is typically in the visible to near-infrared spectra and is collected by the onboard SEM charge-coupled device (CCD) camera. The various CL-signatures corresponding to compositional or structural differences of the interrogated sample and in

combination with BSE, the two image techniques collectively provides a more comprehensive characterization of the sample. One of the primary applications of CL-imaging in zircon studies is the identification of internal growth zonation. As zircon often crystallizes in multiple stages, concentric or sector zoning patterns commonly form which reflect changes in geochemical conditions during nucleation and growth of the crystal. The zonation patterns thus appear as relatively CL-brighter to darker bands. The observed CL-signatures are mainly governed by variations in trace elements content such as rare earth element (REE), and uranium and thorium concentrations. Bright CL zones typically indicate lower concentrations of these trace elements, while dark zones suggest higher levels of REE and/or actinides. In geochronology, CL-imagery is therefore utilized as a preparatory step before U-Pb dating, ensuring that targeted analyses are conducted in domains favorable for the research purpose. Selective domains can thus provide age constraints of the primary crystallization and/or recrystallization ages by avoid areas affected by metamictization or other alteration that might induce U-Pb open system behavior.

7.2.2 Electron backscatter diffraction

Electron backscatter diffraction (EBSD) is a crystallographic acquisition technique used in SEM to analyze microstructural deformation and orientation properties of crystalline materials. The analytical method relies on detecting elastic backscattered electrons that are diffracted during interaction with the atomic lattice of the targeted material. The “captured” elastically backscattered electrons produces Kikuchi patterns if the Bragg’s condition is fulfilled. The Bragg’s law states that diffraction will occur when incident waves reflect off parallel lattice planes at specific angles and collectively reinforce each other to produce the detectable diffraction patterns. If the Bragg’s condition is not fulfilled the constructive interference is hampered wherefore the backscattered electrons will not form well-defined Kikuchi patterns. To achieve optimal EBSD-analysis, the sample must thus be tilted 70° from the horizontal. Because the incident electron beam has a relatively broad angular spread, diffraction occurs over a range of angles rather than at discrete points. This widespread results in the formation of Kikuchi bands instead of sharp Bragg peaks that X-ray diffraction produces. The Kikuchi patterns are the product of all detectable Kikuchi bands within the targeted volume of which represents a gnomonic projection of interrogated crystal lattice planes relative to the *x*-*y*-*z* reference frame of the SEM-stage. Each Kikuchi band corresponds to a specific set of lattice planes within the crystal, were band width and intensity directly related to the atomic spacing and diffraction conditions. Collectively, the Kikuchi bands form the characteristic Kikuchi patterns or the, so-called, electron backscatter pattern (EBSP), which represents the crystallographic symmetry of the sampled region. By comparing the EBPS geometrical arrangements in conjunction with a crystallographic database, it is possible to index and quantify data with high precision. Today, conventional EBSD-analysis can achieve precision of <1° for lattice rotation, and spatial resolution down to c. 10 nm, making this analytical method well suited for analyzing microstructural features such as grain boundaries, sub-grain structures, and lattice distortions. The resolution of EBSD depends on several factors, including the step size between measurement points, the electron beam accelerating voltage (generally kept between 15–25 keV), and the sample’s crystallinity. The capability of EBSD to detect even subtle crystallographic distortions makes it a reliant, fast, and a prominent method for studying impact-induced stress-strain effects in zircon.

To achieve high-quality Kikuchi patterns, EBSD-analysis requires meticulous sample preparation. The technique is highly surface-sensitive, as the interaction volume of utilized backscattered electrons is limited to a sample depth of approximately 50 nm. Any surface roughness, oxidation, or the presence of contaminates can therefore degrade diffraction patterns and reducing data quality and indexing accuracy. Therefore, samples must be carefully polished, with the aim of achieving a mirror-like finish. To attain an optimal finish, final polishing is carried out with mechanical and/or vibrational polishing machines, equipped with a soft polishing cloth used together with a sub-micrometer colloidal silica slurry (<0.25 µm). Likewise, the thickness of the carbon coating is also crucial. If the coating is too thick, the diffraction patterns become weaker, and a too thin coating can generate electron charging effects that obstruct data acquisition. As a general guideline, the coating is kept between 5–10 nm. For optimal pattern quality, the sample is mounted on a 70° pre-tilted specimen holder in the SEM-chamber. Collection and indexing of EBPS-data are performed automatically as defined by the user, and acquisition is executed in a grid configuration within the selected area. Each data point in the grid corresponds to one EBPS whereas the user can regulate the spatial resolution of the overall data grid by defining the spacing between each data point (i.e. step size). A lower step size yields greater resolution but in return extends the analytical time. For

each second, several hundreds to thousands of EBPS can be recorded and indexed, generating a hefty dataset. Data are first post-processed in the selected software(s) (the Oxford software AztecCrystal was mainly used throughout this Ph.D. thesis). The main criterion to ascertain analytical confidence in acquired EBSD-data is accomplished by comparing the mean angle deviation (MAD) of the measurements of the pristine crystal structure (given by the indexing file) of the phase in question (e.g. zircon) to the overall interrogate analyzed area. Adjacent data-points with a MAD-value equal or below 1° is regarded to retain analytical authenticity. Independent of the MAD-criterion, solitary data-points over the scanned grid (so called wild spikes) are treated as analytical artifacts and are removed by applying a "noise reduction" filter during post processing. After data treatment, the construction of various thematic maps and statistical charts are made in order to illustrate and interpretate the crystallographic architecture of analyzed sample.

7.3 Transmission electron microscopy

Similar to SEM, transmission electron microscopy (TEM, Fig. 5e) utilizes accelerated electrons to probe and image localized regions of a material. However, the primary beam of a TEM operates at higher keV (i.e. >100 keV, compared to <30 keV for SEM imagery and EBSD analysis) and therefore can achieve a higher electron momentum (i.e. smaller wavelength). Consequently, accelerated electrons generated in a TEM have the capability to interact with nanoscale regions of the interrogated material, enabling an instrumental resolution down to the picometer-scale (1×10^{-12} m)—thus capable of image single atom columns (e.g. Williams and Carter, 2009). During TEM-analysis two primary modes can be operated—imaging and diffraction. There are various settings in the imaging mode, but the most common mode used operates under the same principal as a SEM: electrons are accelerated within the incident beam, upon impact, electrons interact with atoms within the targeted area causing scattering of electrons which are collected and recorded by the detector and the CCD-camera. Likewise to SEM, the imaging contrast (i.e. the signal intensity) corresponds to the square of the atomic number (z) wherefore heavier elements (e.g. U) produce higher signal intensities compared to lighter elements (e.g. Si). In diffraction mode, post-specimen lenses are used to capture electrons to form diffraction patterns of a crystal. The patterns appear as a periodic array of distinct spots or circular patterns (depending on crystallinity) of which are lattice projections of atomic positions in reciprocal space (i.e. basically an atomic coordination system, *d*-spacing). Collected data enables high-detail interpretation of sub-micrometer features and provides insights into the crystallographic framework.

Sample preparation for TEM analysis is both time consuming and complex work but is an essential part of the technique. For optimal analytical condition it is required that the specimens retain a uniform electron transparency (i.e. <100 nm thickness) to maximize electron scattering and to minimize electron absorption. Nowadays this is achieved by cutting out a thin foil with a focused ion beam (FIB, Fig. 5f) (e.g. Wirth, 2009). As TEM has the capacity to actualize atomic resolution, the technique is favorably applied in the study of crystal interfaces and defects (e.g. sub-grain, twin boundaries, and dislocations) in solid state materials.

7.4 Raman spectroscopy

Raman spectroscopy (Fig. 5g) is a non-destructive analytical technique used to investigate the vibrational, rotational, and other low-frequency modes of molecular bonds. The Raman effect relies on the inelastic scattering of monochromatic light (from various laser-sources, e.g. 532 nm) of which interacts with the molecular vibrations of the interrogated sample. These vibrations result in a shift of energy which provide a fingerprint of the probed material's molecular composition and crystal structure. The process begins with a laser beam directed at the sample. Upon impact, the majority of emitted photons undergo elastic (or Rayleigh) scattering, where the scattered photons retain the same energy as the incident light. However, a small fraction of the photons interacts with the molecular vibrations of the sample, leading to a sharp shift in their energy. This inelastic scattering is what is known as the Raman effect and can result in either a gain or loss of energy which corresponds to Stokes or anti-Stokes Raman scattering, respectively. Stokes scattering, which is more commonly used in Raman spectroscopy, occurs when the scattered photons have lower energy than the incident photons due to energy transfer to the sample. In contrast, anti-Stokes scattering is less intense and involves photons gaining energy from the pre-excited molecular vibrations. The scattered photons are collected by the instrument and are directed through various optical components, including filters and a monochromator, which separate the Raman scattered light from the Rayleigh scattered light. The filtered Raman signals are then dispersed by a diffraction

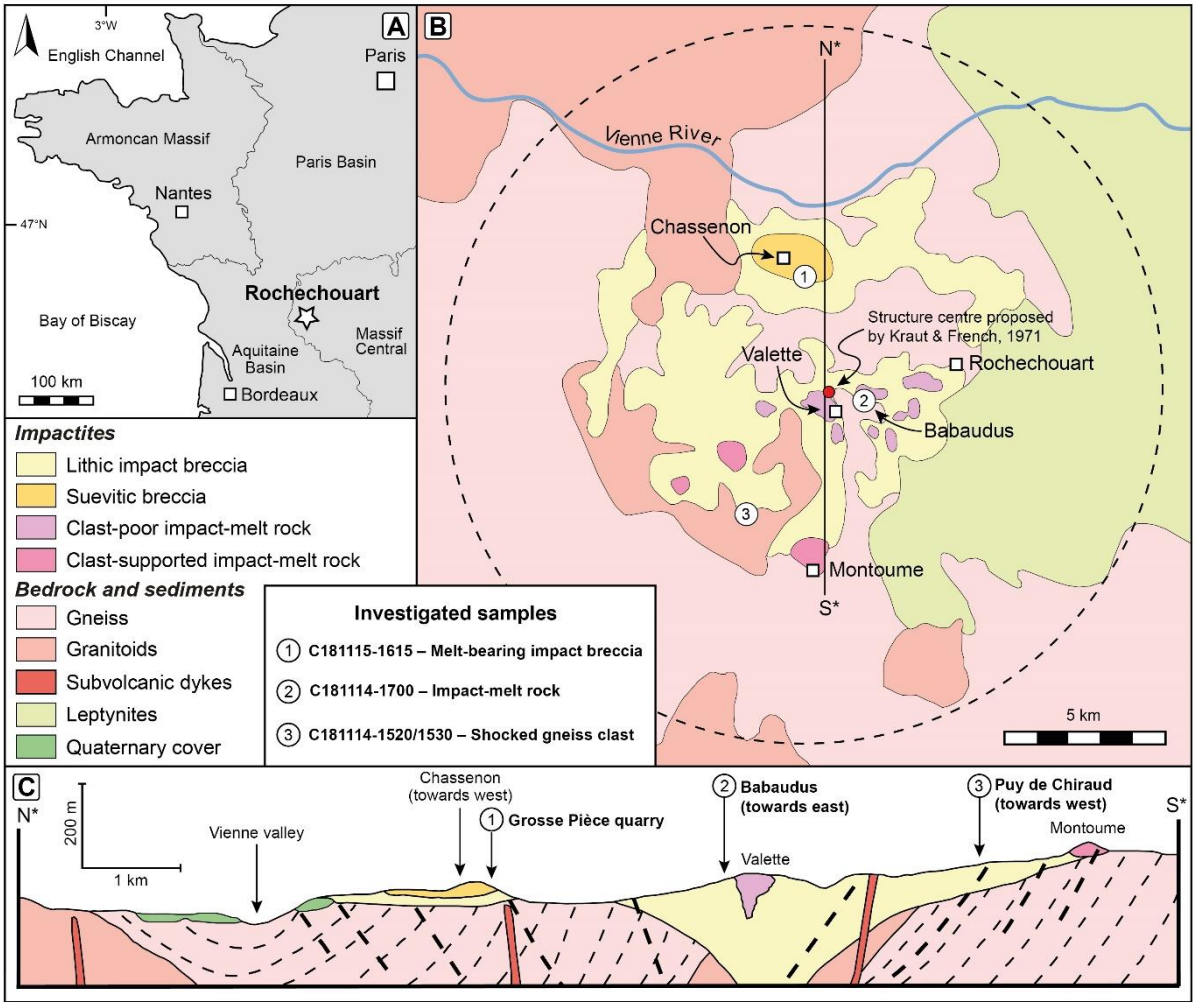

Figure 6. Simplified geological map of the Rochechouart impact structure (B) in southwestern France, with inset indicating the regional location (A). B, C) The map outlines the distribution of impactites and underlying bedrock units (modified after Lambert 2010, Sapers et al., 2014) and the proposed impact structure center by Kraut and French (1971, marked by the red dot). C) Schematic cross section (corresponding to profile N*–S* in B) of the impact structure with the interpreted position of the crater floor and the extent of impactites (modified after Lambert 2010. B–D) The sampling site for (1) the Chassenon suevitic breccia, (2) the Babaudus impact-melt rock, (3) The shocked gneiss clast west of the town Montoume. Cities and towns are marked by squares.

grating and detected by the instrument CCD camera—allowing the Raman spectrum of the targeted area to be recorded. The resulting spectrum consists of several peaks of which corresponds to phonon modes that occur at specific wavelengths (i.e. Raman shift). Collectively, the phonon modes constitute a spectral fingerprint of a specific phase (e.g. zircon). Constraining Raman spectral pattern therefore enables identification of molecular structures, and offers insights into, for example, molecular bonding, and crystallinity.

8. Geological setting and sample material

The Rochechouart impact structure is situated in south-central France (45°500N; 0°460E; Fig. 5) c. 150 km northeast of Bordeaux and resides in 550–300 Ma metamorphosed granitic and gneissic units belonging to the NW margin of the Hercynian Massif Central (Lambert, 2010) (Fig. 5a). Originally the structure was interpreted as a volcanic caldera until the discovery of diagnostic shock features such as shatter cones, shocked quartz and isotropic plagioclase, confirmed

an extraterrestrial origin (Kraut, 1969). The Rochechouart impact structure accounts to one of the largest in western Europe with an estimated pre-erosion ring diameter of <50 km (Lambert, 2010). Due to extensive post-impact erosion, the ring exposure today has been reduced to c. 24 km in diameter (Fig. 5b). As a result, the majority of impactite deposits and morphological crater characteristics (e.g. the central up-lift) have experienced heavy erosion, as far down as to the crater floor (Fig. 5c). However, scattered areas of autochthonous and allochthonous impactite deposits are still preserved, including lithic impact breccias, suevitic breccias, coherent impact melt rocks and fine-grained fallback deposits (i.e. impactoclastite) (Fig. 5b). The age of the impact event has been a matter of debate, with age constraints varying between c. 154 and 214 Ma (Schmieder et al., 2010, and references therin). On the basis of the 214 ± 8 Ma $^{40}Ar/^{39}Ar$ date of impact melt rock from the Rochechouart structure, Spray et al. (1998) propsed a controversial hypothesis of synchronous multiple impact events. Based on the geochronological data at that present time, four impact events has dates which coincided within uncertainty to the Rochechouart impact event: Manicouagan (214±1 Ma), Lac Saint Martin (219 ± 32 Ma), Obolon (215 ± 25 Ma), and Red Wing (200 ± 25 Ma) (Spray et al., 1998). The authors therefore speculated whether a co-working effort of these impact events could have initiated the Carnian-Norian extinction at ~220 Ma. Later on, the newly established $^{40}Ar/^{39}Ar$ 203 ± 2 Ma age of Schmieder et al. (2010) disputed the multiple impact hypothesis. The debate took a new turn, and discussions arose whether the Rochechouart impact event could have been a potential trigger of the end-Triassic extinction. However, with the progressive improvement regarding precision and accuracy of various geochronological methods over the following years, the aforementioned hypothesis has now been abandoned. As-of-today, the most precise and accepted age of the Rochechouart impact event is 206.92 ± 0.32 Ma (2σ, using the $^{40}Ar/^{39}Ar$ incremental step heating method on materials from the Babaudus impact-melt rock, Cohen et al., 2017).

As evident from the distinct potassium enrichments within target rocks, and by post-shock

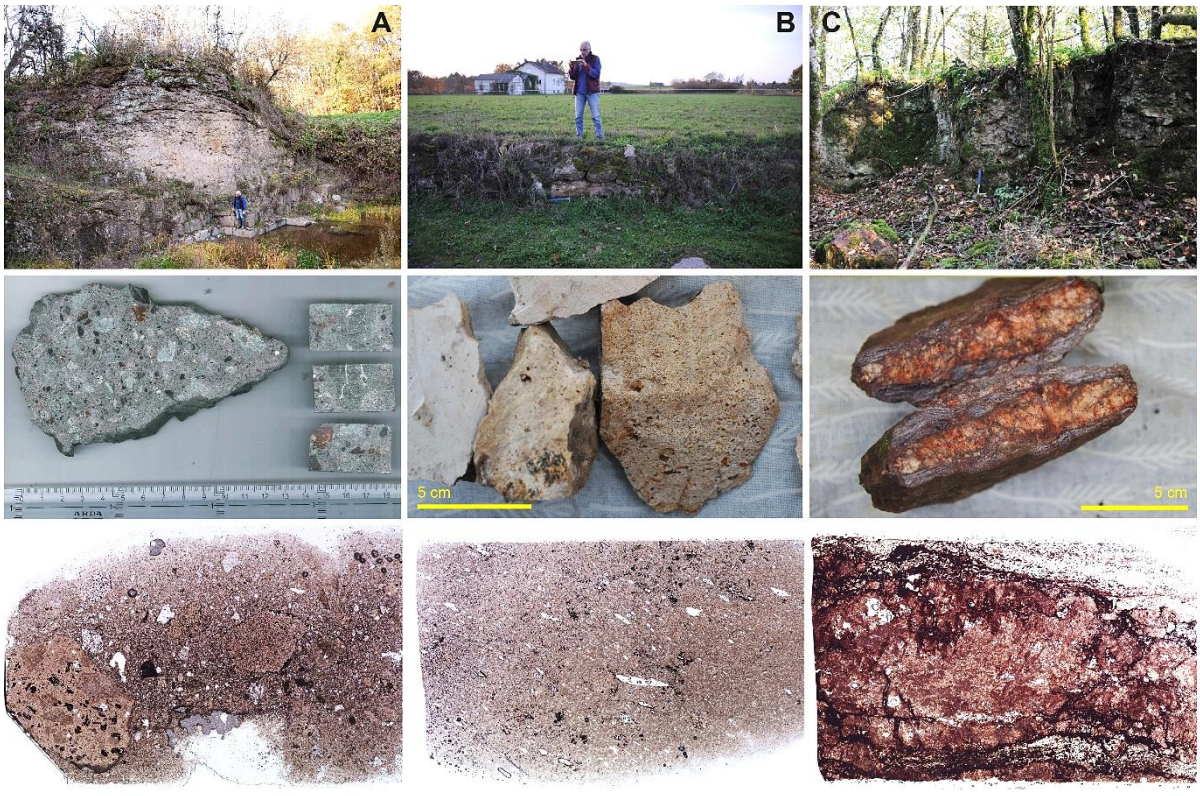

Figure 7. Sampling localities (top row photographs) of the three impactites (A–C correspond to samples 1–3 in figure 5, respectively) that was collected during field work with Philippe Lambert. A) Chassenon suevitic breccia, B) Babaudus impact-melt rock, C) baked gneiss clast from Puy de Chiraud. Mid row photographs) various hand specimens of the three impactites, both polished (A) and fresh (B, C). Bottom row) photomicrographs of the samples, all thin sections were depictured by a high-resolution scanner (note that the colors do not match how they are perceived in reality, this is due to the color code that the scanner program used. (A) is perceived as having a greener hue, (B) is perceived as having a yellow hue.)

argillization of melt and glass clasts, impact-induced K-metasomatism has heavily altered the majority of impactites within the Rochechouart structure (Sapers et al., 2014). However, shock-induced features in major minerals are preserved and, for example, includes: PFs, planar deformation features (PDFs), toasted appearance, ballen, and mosaicism in quartz; kink banding in mica; diaplectic quartz and feldspar glass (Kraut and French, 1971, Lambert, 1977, Trepmann, 2008, Ferriere et al., 2009, Sapers et al., 2014). The wide range of shock pressures recorded in the Rochechouart impactites constraints pressure ranges from a few GPa up to >45 GPa (Lambert 1977).

Prior to this Ph.D. thesis, the only investigation on shock-induced features in zircon includes the study by Rassmussen et al. (2020). Rather than focusing on studying various microtextures in zircon, their aim was to test the zircon U–Pb isotopic system on potentially re-equilibrated domains that were formed during high-temperature-induced recrystallization. Their study was focused on characterized granular zircon in the Babaudus impact-melt rock. Their U–Pb age constrains, via LA-ICP-MS depth profiling, reflects magmatic intrusion (~480 Ma) and metamorphism (~360 Ma) ages within the local region. Some FRIGN zircon grains yielded dates between 204–207 Ma of which indicate partial to complete resetting of the zircon U-Pb system during impact post-shock temperature >1,200 °C. These results further demonstrate that FRIGN zircon is a promising tool for the absolute dating of impact events.

The Rochechouart sample collection that have been investigated over the Ph.D. project represent a broad continuum of exposure to various P–T(–t) conditions. The sample selection was motivated on the basis that the respective impactite should reflect different shock intensities and therefore comprise various zircon shock features. Zircon grains from three different impactites have been studied over the three Ph.D. projects (Fig. 6): 1) The Chassenon suevitic breccia (Fig. 7a). 2) The Babaudus impact-melt rock (Fig. 7b). 3) A highly shocked ("baked") gneiss clast embedded in a suevitic breccia at Puy de Chiraud (Fig. 7c).

9. Summary of papers

The author's contribution to each paper is given in Table 1.

Paper I

Anders Plan, Gavin G. Kenny, Timmons M. Erickson, Paula Lindgren, Carl Alwmark, Sanna Holm-alwmark, Philippe Lambert, Anders Schersten, Ulf Söderlund. (2021), *Exceptional preservation of reidite in the Rochechouart impact structure, France: New insights into shock deformation and phase transition of zircon.* Meteoritics & Planetary Science, *56*:1795–1828.

This study presents a detailed investigation of shock-induced microstructures in zircon grains from the Chassenon suevitic breccia. Through SEM imaging and EBSD analysis, we documented an unprecedented degree of reidite preservation, with some grains exhibiting near-complete to complete transformation to the high-pressure $ZrSiO_4$ polymorph, reidite. Our findings reveal the presence of five distinct reidite variants or habits, including the commonly observed lamellae and granular habits, as well as three newly identified morphologies: blade, wedge, and massive domains. Like observation from high-P experiment, these various reidite habits are interpreted as being products of relatively higher shock intensities, where reidite morphology becomes bulkier and coherent as a result. These novel reidite habits further crosscut and offset one another in systematic relationships. The observation indicates that reidite can form at multiple stages throughout an impact event—both during shock compression and decompression. Twinning in both zircon and reidite was identified in this study, with {112} reidite micro-twin of which exhibit a 65° misorientation about the <110> axis, similar to shocked twinning in zircon. The development of these twins is most pronounced in grains containing high proportions of reidite, suggesting that this twin type preferentially forms under relatively high pressures, therefore is mainly linked to wedge and domain type reidite. The systematic crosscutting relationships between {112} reidite twins and other reidite domains indicate that twinning represents a late-stage feature, forming after initial reidite formation, occurring during the shock release. The study further explores

the conditions under which reidite reverts back to zircon. We identified the presence of FRIGN zircon, a distinct recrystallization texture that retains systematic crystallographic imprints of its precursor reidite. We demonstrate that this transformation occurs when zircon experiences prolonged exposure to temperatures exceeding 1,200°C, leading to full recrystallization into a granular state. However, if the temperature excursion is short lived, partial reidite → zircon reversion transpires. This study accounts to the first documentation of such process, denoted as zircon reversion fronts (ZRF). The ZRF appear as migrating boundary where zircon begins to recrystallize at the expanse of reidite. The formation of these ZRF suggests that the grains underwent brief but intense heating, likely in proximity to impact melt material. Hence accomplice localized and partial recrystallization of reidite without completing a full reversion into FRIGN zircon.

Paper II

Anders Plan, Sanna Alwmark, Ryan S. Jakubek, William R. Hyde, Aaron J. Cavosie, Timmons M. Erickson. (submitted manuscript, March 2025), *On the Raman spectra of shock metamorphosed zircon – spectral characterization, challenges, and recommended practice.* American Mineralogist.

This study presents a comprehensive investigation of the zircon Raman spectral response over various extreme pressure-temperature conditions associated with impact metamorphism. By combining SEM-imagery (BSE and CL), EBSD analysis, and Raman spectroscopy, the study examines the zircon → reidite → zircon phase transition and the associated spectral characteristics. Shocked zircon grains from the Chassenon suevitic breccia and the Babaudus impact melt rock were here used and compared to the 91500 zircon standard reference material. The findings provide a detailed framework for more accurate interpretation of complex Raman spectra of shock-metamorphosed zircon and highlight the challenges in distinguishing true reidite spectral signals from interfering phenomenon that can yield Raman peaks proximal to reidite. The investigated zircon grains have experienced pressures ranging from 23 GPa to >53 GPa (various reidite habits), and temperatures >1,200°C (various FRIGN zircon grains). Peak fitting of Raman spectra where performed, and reveals systematic trends in phonon mode modification, characterized by progressive peak broadening and shifts towards lower wavenumbers with increasing shock intensity. These spectral changes are interpreted as a function of exposure to increasing strain tensors that arise from shock deformation processes. Compared to reidite, the FRIGN zircon grains display a higher degree of spectral adjustments. The intensity of strain subjected to FRIGN zircon grains was thus more extensive, and presumably corresponds to eigenstrain generated during post-shock heating. Another critical finding of this study is that REE^{3+} photoluminescence emissions can interfere with $ZrSiO_4$ Raman spectra, potentially leading to misidentifications of reidite. Given that Raman signals from REE^{3+} overlap with various key phonon modes of $ZrSiO_4$, the study highlights the necessity of careful peak assignments to avoid erroneous interpretations. We conducted an extensive $ZrSiO_4$ Raman literature review to build up a reference library of $ZrSiO_4$ phonon mode positions, evaluating over 100 Raman spectra from previous publications. We noted that previous studies which have identified reidite solely based on Raman spectroscopy may need to be re-evaluated to confirm the presence of reidite independently, we address one study as an example. Additionally, the study highlights the importance of selecting appropriate laser excitation wavelengths when preforming Raman analysis. This can be of great importance since the 532 nm lasers tend to produce photoluminescence effects that may interfere with Raman peaks. To mitigate such misinterpretations in future studies, our study formulated a recommended methodology to accurately evaluate shocked $ZrSiO_4$ Raman spectra. This study further documents that the zircon-to-reidite phase transition is often incomplete, as demonstrated by Raman spectroscopy detecting preserved zircon domains within reidite-bearing grains that were unresolved by EBSD. This suggests that zircon does not fully transform to reidite, regardless of P-T conditions favoring the reidite stability field—in support of observation from high-P experiments. Furthermore, we identify a Raman peak at 450 cm^{-1}, which systematically reoccurs in domain habits of reidite. This peak is here hypothesized to represent the intermediate high-pressure low-symmetry phase (experimentally produced) that serves as a structural bridge in the zircon-to-reidite transformation. Additionally, two distinct Raman peaks at ~730 cm^{-1} and ~780 cm^{-1} are also systematically observed. Likewise, these are exclusive to reidite spectra, and may correspond to unknown high-P polymorphs (previously discussed in a study) or represent nano-crystalline phases formed during impact metamorphism (as previously observed in shock recovery experiments).

Table 1. Author contribution

	Paper I	Paper II	Paper III
Study design and concept	**A. Plan**	**A. Plan**	**A. Plan**
Data collection and analysis			
Field work and sampling	**A. Plan** P. Lambert	**A. Plan** P. Lambert	**A. Plan** P. Lambert
Mineral separation	**A. Plan**	**A. Plan**	**A. Plan**
Sample preparation for SEM-EBSD analysis	**A. Plan** G. Kenny	**A. Plan**	**A. Plan**
Sample preparation (FIB) for TEM analysis	—	—	B. Cymes **A. Plan** T. Erickson
SEM-imagery	**A. Plan**	**A. Plan**	**A. Plan**
SEM-EBSD analysis	**A. Plan** G. Kenny	**A. Plan** W. Hyde	**A. Plan** T. Erickson (TKD)
TEM analysis	—	—	R. Christoffersen B. Cymes T. Erickson **A. Plan**
Raman spectroscopy analysis	—	**A. Plan**	—
Optical microscopy	**A. Plan** S. Alwmark C. Alwmark	**A. Plan**	**A. Plan** S. Alwmark
Data handling			
Data (post-)processing	**A. Plan** T. Erickson	**A. Plan**	**A. Plan** R. Christoffersen
Data interpretation	**A. Plan** T. Erickson G. Kenny P. Lindgren S. Alwmark C. Alwmark	**A. Plan** R. Jakubek S. Alwmark W. Hyde	**A. Plan** W. Hyde S. Alwmark T. Erickson
Manuscript handling			
Figures, illustrations and tables	**A. Plan**	**A. Plan**	**A. Plan**
Writing: original draft	**A. Plan**	**A. Plan**	**A. Plan**
Writing: review and editing	**A. Plan** T. Erickson G. Kenny P. Lindgren S. Alwmark C. Alwmark U. Söderlund A. Schersten	**A. Plan** R. Jakubek S. Alwmark W. Hyde A. Cavosie T. Erickson	**A. Plan** S. Alwmark W. Hyde T. Erickson

Paper III

Anders Plan, Timmons M. Erickson, William Hyde, Sanna Alwmark, Roy Christoffersen, Brittany Cymes. (Manuscript), *Shock-induced Zircon Recrystallization Mediated by Shear Localization.*

This study investigates how zircon undergoes recrystallization mediated via shear localization that is generated under extreme conditions during hypervelocity impact. We have here examined zircon grains from a specific impactite unite within the Rochechouart impact structure, that host an abundance of narrow micrometer-scale planar deformation features—here termed granular neoblastic shear bands (GNSBs). These features act as focal sites for extreme strain accommodation and subsequent dynamic recovery. Using integrated SEM imaging (BSE and CL), EBSD (including TKD), and high-resolution TEM, we trace a progressive microstructural evolution within these GNSBs, from dislocation-dominated regime to the emergence of (sub-)micrometer zircon neoblasts. These neoblasts reflect the culmination of a deformation-to-recovery transition.

Initially, the zircon system responded to shock loading through the activation of multiple slip systems, forming dense networks of dislocations and a-plane stacking faults. With continued deformation, dislocations reorganize into sub-grain structures and dislocation cells, leading to the development of low- and high-angle boundaries. The recrystallization mechanism to zircon neoblasts, likely, was facilitated by sub-grain rotation and/or grain boundary migration. Key to this transformation is the thermomechanical feedback process of adiabatic “shear” heating, under which the extreme imposed strain rates and the accompanied mechanical work was rapidly converted into localized heat within the GNSBs. Thus, raising temperatures above 1,675 °C in confined deformation zones, without any time for thermal dissipation—wherefore defined as adiabatic heating. This localized heating not only enables dynamic recrystallization but also promotes thermal softening and enhanced grain boundary mobility. The cuspate-lobate morphologies observed at the boundaries between GNSBs, and the zircon matrix provide direct evidence for this thermally assisted recrystallization pathway. The presence of zircon dissociation into ZrO_2 further constrains the internal temperature gradient and reinforce that the recrystallization was not driven by external heat sources but arose from internally generated heat.

Crystallographic data show dispersed misorientations in pole figures—similar, yet not identical, to patterns observed in FRIGN zircon—suggesting that GNSBs may represent hybrid microstructures formed through the interaction of twinning, reidite reversion, and adiabatic shear localization. The progressive widening of GNSBs within grains, from narrow bands to fully recrystallized interiors, highlights the dynamic nature of the process and the potential to completely transform the zircon structure. Collectively, these findings establish GNSBs as a new class of shock-induced microstructures in zircon and propose them as natural analogues to adiabatic shear bands, a well-known deformation process described in material science. This research therefore provides a crucial step forward in decoding the coupled mechanical and thermal deformation mechanisms that govern the response of zircon during impact metamorphism.

10. Discussion – a crystallographic monologue

Insights into $ZrSiO_4$ conversion and reversion

The findings presented in paper I mark a significant advancement in understanding crystallographic response of $ZrSiO_4$ under shock metamorphic conditions, allowing for a refined reconstruction of the shock history of $ZrSiO_4$. Five reidite habits—lamella, granular, blade, wedge, and massive domains—and their associated micro-twin, and reversion features were documented. The three latter habits are novel variants, characterized for the first time in this study. Their distinct crystallographic orientations and topotactic relationships further suggest that the formation of different reidite morphologies may be governed by increasing shock intensities. Therefore, these five habits reflect exposure to various shock intensities (i.e. pressure conditions), with morphologies becoming bulkier as pressure increases. The reidite → zircon reversion textures, FRIGN zircon and ZRF, reflect the post-shock thermal evolution of the investigated grains. The presence of bulk reidite-bearing grains highlights the importance

of quenching rates in reidite preservation, as extended exposure to sufficiently high temperatures (i.e. >1,200°C) would otherwise drive complete reversion of reidite to zircon (i.e. FRIGN zircon), whilst a short-lived thermal pulse would halt the process and form partial reverted domains (i.e. ZRF). These textures embody the concept of phase heritage, in which the crystallographic memory of high-pressure reidite is preserved through systematic orientation relationships in the reverted zircon. The coexistence of massive reidite with ZRFs—neoblastic zircon fronts exhibiting orthogonal misorientations—is therefore consistent with reidite reversion. As the crystallographic configuration is observed both in partially reverted grains (ZRFs) and in fully granular (FRIGN) zircon, it reinforces the interpretation that these textures represent progressive reversion products of reidite. Shortly after the publication of this study, an alternative recrystallization model was proposed. Kovaleva et al. (2021) challenged the FRIGN zircon model and the view that granular neoblastic zircon forms through a solid-state reversion of reidite. This model posits that granular zircon textures can originate from the complete incongruent melting of zircon followed by crystallization from unmixed silicate and oxide melts during cooling. Crucially, this model involves a melting–recrystallization pathway which produce granular zircon with systematic orientations resembling FRIGN zircon, but without requiring a reidite precursor. However, the link between FRIGN zircon and ZRF corroborates the concept of phase heritage and in extension, this study provides, for the first time, support to the FRIGN zircon model.

These new records of microstructures provide valuable constraints for interpreting the general deformation sequence and $ZrSiO_4$ phase transitioning, from initial undeformed zircon at pre-impact conditions, through progressive phase transformations during shock compression (zircon → reidite) and the ensuing decompression (shocked micro-twins in both zircon and reidite), to reidite → zircon reversion mechanisms in form of solid-state recrystallization during the post-impact regime (ZRF → FRIGN zircon).

Assessing Raman spectroscopy as a tool for evaluating shocked zircon

As discussed in paper II, the findings of this study have broad implications for evaluations of $ZrSiO_4$ Raman pattern and for the identification of reidite by Raman spectroscopy. This study characterized systematic Raman spectral trends that provide new insights into how zircon records and respond over a wide variety of impact metamorphic conditions. As demonstrated in paper II, interpretation of zircon Raman spectra is a complex procedure with many pitfalls that can lead to wrongful misinterpretations regarding high-P phases. Over 100 Raman spectra from previous high P-T $ZrSiO_4$ studies were here investigated, amounting to the most comprehensive Raman spectral dataset of $ZrSiO_4$ (from both natural settings, high P-T experiments, material from atomic bomb test site, *Ab Initio* calculation). Based on the study results and the literature review, Raman peak position of systematically reoccurring bands and zircon and reidite phonon mode where pinpointed. Based on this collection and our results, a reliable methodology for interpreting complex $ZrSiO_4$ Raman spectra was established. By utilizing the formulated practice, we hope to aid future investigations of potentially shocked zircon and mitigate erroneous $ZrSiO_4$ Raman interpretation. Beneficially, the developed method can also be applied to identify and interpret other phases than zircon and reidite. This research therefore contributes to refining the use of Raman spectroscopy as a diagnostic tool in planetary science as the practice assists towards a more refine approach for constraining high-pressure mineral phases. The identification of potential intermediate phases (HPLS phase) and other unknown polymorphs discussed in paper II further expands our understanding of the shock behavior and phase transitioning of $ZrSiO_4$ and emphasizes the need for continued experimental and natural sample investigations to unravel the full complexity of zircon → reidite → zircon phase transitioning.

Erroneous Raman interpretations of reidite – a literature example

Determining the presence of reidite can be of great importance since the mineral accounts as diagnostic evidence of hypervelocity impact and provides thermobarometric markers that can be utilized to calibrate shock metamorphic conditions. In paper II, we critically assessed and discussed a previous study, published in a well renowned journal, that has misinterpreted various Raman bands as reidite, and claimed the identification of new impact ejecta deposit in Western Scottland. Here we incorporate results from the three paper of this thesis (paper I–III) to expand this discussion further.

Based on Raman spectroscopy (using a 532 nm laser excitation source) and microscopic imagery, Drake et al. (2017) claims to resolve the presence of reidite (lamella habits) in zircon grains from two locations in the Isle of Skye, northwestern Scotland. Firstly, microscopic images of the study are here examined, as microtextural features can infer the presence of reidite. The study provides a cross-polarized light (XPL) photomicrograph of one of the two zircon grains, and a CL-image of the other grain, both are interpreted as having "*reidite shock lamellae*" (Drake et al. 2017, their Fig. 3a and 4a). Upon inspection, resolving the "*shock lamellae*" in the XPL-image is no easy task. Indeed, the zircon grain is fractured in a chess-like pattern (Drake et al. 2017, their Fig. 3a) but the diagonal markings have no XPL resemblance of reidite lamellae in, for example, Erickson et al. (2017, their Fig. 3). In SEM-imagery, reidite lamellae have been observed to occur in several direction on the polished surface, are consecutively stacked, and seldom occurs as a single lamella. The spacing between each lamella is generally between ~1–5 μm and is accompanied by fractures in the zircon matrix that are oriented parallel to the reidite lamellae (presumably extension fractures that formed during decompression) (Plan et al., 2021, 2025, paper I–III). Due to being ~10% denser, the *z*-contrast of reidite is BSE-brighter compared to zircon, and reidite with planar habits (lamella and blade) have dark CL-signature (Plan et al., 2021, paper I). Figure 4a of Drake et al. (2017) depictures a zircon grain in CL that comprise, according to their interpretations, four single "*crosscutting reidite-containing lamellae*". The figure markings (Drake et al., 2017, their Fig. 4a, A–D) of the planar-like features have bright CL-signatures, occurs as single planar features having four different orientations. The zircon matrix is otherwise pristine, having no additional fractures related to the marked planar features (Plan et al., 2025, paper III). As there is no apparent sign of plastic deformation related to impact metamorphism, it is implausible that the zircon matrix would be intact if the grain was subjected to minimum 23 GPa compression-decompression conditions. None of the archetypal reidite lamella characteristics from previous studies match this grain (Plan et al., 2021, 2025, paper I–III), instead the planar features resemblance surface scratches induced by mechanical polishing (Drake et al., 2017, their Fig. 4a). Hence, the provided contextual data do not support that the zircon grains are reidite-bearing.

Secondly and foremostly, the Raman data of Drake et al. (2017) are reviewed. The results are summarized in the main text as: "*our sample bands and peaks accord well with all known natural reidite Raman bands*" (Drake et al., 2017; their Fig. DR4, Tab. DR5). Their table DR5 provides one zircon Raman spectra that resolves thirteen peaks that are compared to a handful of previous Raman studies of shocked zircon. As tabulated (Drake et al., 2017; their Tab. DR5), 9 Raman peaks are interpreted as zircon peaks positions at ω: 202, 214, 228, 352, 433, 548, 638, 970, and 1007, in proximal agreement to peak positions of previous Raman study of zircon (Plan et al., 2021, 2025, paper II). The four remaining bands are interpreted to correspond to reidite, with ω: 552, 822, 868, 1001. Note that out of the 13 active reidite phonon mode (e.g. Stangarone et al., 2019, Mihailova et al., 2019), the authors only attribute four peaks to reidite. Raman studies, prior to 2017, on natural shocked zircon have spectra that resolve more than four reidite Raman peaks (e.g. Wittmann et al., 2006, Chen et al., 2013). However, such studies are not included and compared in their table DR5 (Drake et al. 2017). As reidite has no active phonon modes at 1001 cm^{-1} (e.g. Stangarone et al., 2019, Mihailova et al., 2019, cf. Plan et al., 2025, paper II), this Raman band is wrongly assigned to reidite. The 552 cm^{-1} peak are proximal to phonon mode Eg $(4)_{reidite}$ and Eg $(4)_{zircon}$ in grain B156 ω ~549 (Plan et al., 2025, paper II, Tab. 1, S1; Fig. 3–4). Since other more intense reidite peaks are absent, it is therefore more likely that this Raman band represents artefacts or another mineral phase. The Raman peaks at 822 cm^{-1} and 868 cm^{-1} are assigned as the strongest support of reidite according to Drake et al. (2017, Tab. DR5, and highlighted in their Fig. DR4). As discussed in Plan et al. (2025, paper II), the position of these two peaks correlates with REE^{3+} photoluminescence emission bands that are readily generated by 532 nm lasers Raman systems. To demonstrate that similar Raman bands of unshocked zircon are frequently resolved by such systems, one spectrum of Drake et al. (2017, their Fig. DR4, reidite site 1) was compared to a FRIGN zircon and the reidite-bearing grains of paper II, and to other zircon grains known to have been unaffected by shock metamorphic conditions (Plan et al. 2025, Fig. 5, paper II). All the examined none reidite-bearing zircon grains display peaks positioned at ω: ~410, ~470, ~505, ~625, ~705, ~785, ~820, ~870, and all but one spectrum resolve a peak close to ~550 (Plan et al. 2025, Fig. 5, paper II). Furthermore, several other examples that used a 532 nm Raman system resolve the same peaks exists in the RRUFF database (RRUFF ID: R050286, R050488, R100144, and R050203; examine the "broad scan with spectral artifacts", note that all spectra exhibit the same distinct peak cluster between 800–900 cm^{-1} that are resolved in Plan et al. 2025, Fig. 5, paper II).

In conclusion, there are no compelling evidence that the zircon grains of Drake et al. (2017) contain reidite or were subjected to shock pressures of ~23 GPa, neither from Raman spectroscopy nor microscopic imaging. By using the recommended Raman spectroscopy practice developed in the paper II study, misinterpretation regarding Raman peaks and $ZrSiO_4$ phases can thus be avoided.

Shearing and recrystallization – a most shocking tale

The findings presented in this study (paper III) mark a substantial expansion in the understanding of deformation and recovery processes in shocked $ZrSiO_4$, and offers new perspective on how zircon accommodates strain and reorganizes its lattice under the extreme conditions associated with hypervelocity impact. While the microstructural and crystallographic response of zircon to impact metamorphism is commonly defined by the formation of planar features, {112] twins, and high-pressure reidite transformation—our documentation of granular neoblastic shear bands (GNSBs) introduces a new deformation regime, shaped by high-strain-rate, shear localization and thermally assisted microstructural evolution and recrystallization

This work reveals that zircon can undergo dynamic recrystallization, presumably by sub-grain rotation and/or grain boundary migration. These features presumably form as a direct product of extreme strain partitioning within the zircon lattice—confined to narrow micrometer-scale shear zones. When subjected to the extreme localized mechanical work, adiabatic heating can occur. The internal crystallographic architecture of the characterized GNSBs reflects a systematic progression: from high-density of chaotic dislocation within the host matrix, to self-reorganization into dislocation wall and cellular features. At a later stage, these features evolved into low- to high-angle boundaries which progressed into sub-grain and eventual developed of strain-free neoblasts. These neoblasts exhibit widely dispersed disorientations (up to 95°) and cuspate-lobate grain boundaries, indicative of dynamic recrystallization facilitated by localized temperature excursion and thermal softening. The occurrence of ZrO_2 confined within the GNSBs constrains the internal temperature gradient to >1,675 °C, suggesting that the recrystallization process was not driven by external conductive heat, but instead by localized shear heating consistent with an adiabatic process. This thermomechanical feedback loop—where mechanical work is rapidly converted to heat which acted as a drive force to the observed microstructural evolution—is a defining hallmark of adiabatic shear band (ABS) in characterized in material science. Our study demonstrates that zircon, despite its refractory and anisotropic nature, is capable of undergoing similar processes during impact cratering. The progression from dislocation regime to dynamic recrystallization documented here closely mirrors various process associated with ASB in a wide range of metals and alloy (Meyers et al., 2003; Xu and Meyers, 2012). The occurrence of GNSBs can therefore be regarded as an geological analogue of such features—hitherto unrecognized in natural materials. This realization offers insights to the behavior of zircon during impact metamorphism—demonstrating that grain refinement and crystallographic reorganization can occur via strain-induced recrystallization pathways, independent of an external heat source (e.g. from invading impact melt components).

Interestingly, the crystallographic fingerprint of GNSBs—particularly the dispersed orientation clusters observed in pole figures closely resembles FRIGN zircon systematic, which is commonly attributed to the solid-state reversion of reidite. Zircon with FRIGN systematics typically retains topotactic misorientation clusters, formed through zircon → reidite → zircon transitions during the post-shock recrystallization. In contrast, the GNSBs described here exhibit less tightly pole clusters where dispersion can range from 65° up to 110°. These discrepancies raise the possibility that GNSBs may represent a hybrid feature—formed through the convergence of multiple deformation mechanisms operating over short spatial and temporal scales during shock compression and/or decompression. Two novel models are here proposed to explain the origin of these textures.

The first model envisions GNSBs as the product of recrystallization from pre-existing shock-induced zircon features—such as {112} twins, reidite lamellae, or amorphous domains analogous to diaplectic glass. In this scenario, the precursor structures are already structurally unstable due to intense deformation—rendering these features highly susceptible to recrystallization. Recrystallization may therefore be initiated by a post-shock thermal pulse, potentially sourced from surrounding impact melt and/or elevated local temperatures excursion following decompression (e.g. generated by the release of store strain energy), which facilitates the means of structural recovery. The presence of dispersed yet

systematic pole figure clusters reminiscent of FRIGN zircon, along with the frequent spatial association of GNSBs with micro-twins and reidite-like morphologies (i.e. some GNSBs resembles reidite lamella, some micro-twins), supports this interpretation. Suggestively, some GNSBs could thus represent recrystallized textures indicative of inherited crystallographic records from reversion of both micro-twins and reidite. This would further explain the pole figure data, were 90° and 65°pole cluster dispersion represent reversion of reidite and micro-twins, respectively.

The second model proposes that GNSBs formed as a direct result of shear localization under adiabatic heating conditions. In this model, the extreme strain-rates lead to mechanical work that rapidly converts into heat, promoting recrystallization locally within the shear zones, through sub-grain rotation and/or grain boundary migration. This is supported by the internal crystallographic progression and microstructural evolution characterized over the data sets. In a step-wise approach, the evolution entails: disorganized dislocation regime that eventually self-reorganized into more orderly features (i.e. dislocation walls and cells). These structures eventually formed low- and high-angle boundaries, and ultimately transitioned to sub-grain into strain-free neoblasts, occurring at a misorientation threshold >10°. The presence of cuspate-lobate grain boundaries observed at the border between the host matrix and the GNSBs indicate thermally assisted boundary migration. A high temperature regime can be further inferred by the $ZrO2_2$ inclusions within the shear zones. These features collectively point toward a deformation pathway that is analogous to ASB, where strain-induced heating acts as a feedback mechanism that promotes microstructural evolution, various deformation phenomena (e.g. deformation twinning and phase transition), recrystallization, and grain refinement.

This interpretation not only extends our understanding of zircon's structural response to hypervelocity impact, but also positions GNSBs as a unique microstructural fingerprint of coupled thermomechanical processes which preserves the interplay between shock-induced instability, thermal feedback, and dynamic recovery in a single, coherent crystallographic fabric.

The tetragonal epilogue

The collective findings presented throughout this thesis mark a notable advancement in the field of impact metamorphism and mineral physics related to the $ZrSiO_4$ system, particularly with regard to decipher the complex of phase transitioning (zircon → reidite → zircon). By integrating microstructural, crystallographic, and spectroscopic approaches, this work refines the framework through which the deformation history of zircon can be interpreted—from progression through high-pressure polymorphs, to the $ZrSiO_4$ pathways of reversion and recrystallization. The recognition of, for example, novel reidite morphologies, partial reversion of reidite into FRIGN zircon domain (i.e. ZRF), improved Raman spectral diagnostics, and the identification of granular neoblastic shear bands all contribute to a more nuanced understanding of how zircon records, responds to, and recovers from impact metamorphic conditions. These results not only improve our ability to reconstruct pressure-temperature-time conditions in impact settings, but also highlights the utility of zircon as a recorder of short-lived, high-energy geological events—hypervelocity impact collisions.

References

Abramov, O. & Mojzsis, S. J. 2009. Microbial habitability of the Hadean Earth during the late heavy bombardment. *Nature,* 459**,** 419-422.

Alvarez, L. W., Alvarez, W., ASARO, F. & MICHEL, H. V. 1980. Extraterrestrial cause for the cretaceous-tertiary extinction. *Science,* 208**,** 1095-108.

Bar-Nun, A., Bar-Nun, N., Bauer, S. H. & Sagan, C. 1970. Shock synthesis of amino acids in simulated primitive environments. *Science,* 168**,** 470-3.

Bohor, B. F., Betterton, W. J. & Krogh, T. E. 1993. Impact-shocked zircons: discovery of shock-induced textures reflecting increasing degrees of shock metamorphism. *Earth and Planetary Science Letters,* 119**,** 419-424.

Butterman, W. C. & Foster, W. R. 1967. Zircon Stability and the Zr02-Si02 Phase Diagram. *American Mineralogist,* 52**,** 880-885.

Callahan, M.P., Smith, K.E., Cleaves, H.J., Ruzicka, J., Stern, J.C., Glavin, D.P., House, C.H. & Dworkin, J.P. (2011) Carbonaceous meteorites contain a wide range of extraterrestrial nucleobases. *Proceedings of the National Academy of Sciences*, 108, 13995.

Cavosie, A.J., Biren, M.B., Hodges, K.V., Wartho, J.-A., Horton, J.W., Jr. & Koeberl, C. (2020)

Dendritic reidite from the Chesapeake Bay impact horizon, Ocean Drilling Program Site 1073 (offshore northeastern USA): A fingerprint of distal ejecta? *Geology* (in press or volume/page pending if not listed).

Cavosie, A.J., Quintero, R.R., Radovan, H.A. & Moser, D.E. (2010) A record of ancient cataclysm in modern sand: Shock microstructures in detrital minerals from the Vaal River, Vredefort Dome, South Africa. *GSA Bulletin*, 122, 1968–1980.

Cavosie, A.J., Timms, N.E., Erickson, T.M., Hagerty, J.J. & Hörz, F. (2016) Transformations to granular zircon revealed: Twinning, reidite, and ZrO_2 in shocked zircon from Meteor Crater (Arizona, USA). *Geology*, 44, 703–706.

Cavosie, A.J., Timms, N.E., Erickson, T.M. & Koeberl, C. (2017) New clues from Earth's most elusive impact crater: Evidence of reidite in Australasian tektites from Thailand. *Geology*, 46, 203–206.

Cavosie, A.J., Timms, N.E., Ferrière, L. & Rochette, P. (2018) FRIGN zircon—The only terrestrial mineral diagnostic of high-pressure and high-temperature shock deformation. *Geology*, 46, 891–894.

Chakoumakos, B.C., Murakami, T., Lumpkin, G.R. & Ewing, R.C. (1987) Alpha-decay–induced fracturing in zircon: The transition from the crystalline to the metamict state. *Science*, 236, 1556.

Chan, Q.H.S., Zolensky, M.E., Kebukawa, Y., Fries, M., Ito, M., Steele, A., Rahman, Z., Nakato, A., Kilcoyne, A.L.D., Suga, H., Takahashi, Y., Takeichi, Y. & Mase, K. (2018) Organic matter in extraterrestrial water-bearing salt crystals. *Science Advances*, 4, eaao3521.

Chyba, C.F. (1990) Impact delivery and erosion of planetary oceans in the early inner Solar System. *Nature*, 343, 129–133.

Cobb, A.K. & Pudritz, R.E. (2014) Nature's starships. I. Observed abundance and relative frequencies of amino acids in meteorites. *The Astrophysical Journal*, 783, 140.

Cohen, B.E., Mark, D.F., Lee, M.R. & Simpson, S.L. (2017) A new high-precision $^{40}Ar/^{39}Ar$ age for the Rochechouart impact structure: At least 5 Ma older than the Triassic–Jurassic boundary. *Meteoritics & Planetary Science*, 52, 1600–1611.

Corfu, F., Hanchar, J.M., Hoskin, P.W.O. & Kinny, P. (2003) Atlas of zircon textures. *Reviews in Mineralogy and Geochemistry*, 53, 469–500.

Costa, M.M., Jensen, N.K., Bouvier, L.C., Connelly, J.N., Mikouchi, T., Horstwood, M.S.A., Suuronen, J.-P., Moynier, F., Deng, Z., Agranier, A., Martin, L.A.J., Johnson, T.E., Nemchin, A.A. & Bizzarro, M. (2020) The internal structure and geodynamics of Mars inferred from a 4.2-Gyr zircon record. *Proceedings of the National Academy of Sciences*, 117, 30973–30979.

Cox, M.A., Cavosie, A.J., Bland, P.A., Miljković, K. & Wingate, M.T.D. (2018) Microstructural dynamics of central uplifts: Reidite offset by zircon twins at the Woodleigh impact structure, Australia. *Geology*, 46, 983–986.

Davis, D.W., Krogh, T.E. & Williams, I.S. (2003) Historical development of zircon geochronology. *Reviews in Mineralogy and Geochemistry*, 53, 145–181.

Drake, S.M., Beard, A.D., Jones, A.P., Brown, D.J., Fortes, A.D., Millar, I.L., Carter, A., Baca, J. & Downes, H. (2017) Discovery of a meteoritic ejecta layer containing unmelted impactor fragments at the base of Paleocene lavas, Isle of Skye, Scotland. *Geology*, 46, 171–174.

Erickson, T.M., Cavosie, A.J., Moser, D.E., Barker, I.R. & Radovan, H.A. (2013) Correlating planar microstructures in shocked zircon from the Vredefort Dome at multiple scales: Crystallographic modeling, external and internal imaging, and EBSD structural analysis. *American Mineralogist*, 98, 53–65.

Erickson, T.M., Kirkland, C.L., Timms, N.E., Cavosie, A.J. & Davison, T.M. (2020) Precise radiometric age establishes Yarrabubba, Western Australia, as Earth's oldest recognised meteorite impact structure. *Nature Communications*, 11, 300.

Erickson, T.M., Pearce, M.A., Reddy, S.M., Timms, N.E., Cavosie, A.J., Bourdet, J., Rickard, W.D.A. & Nemchin, A.A. (2017) Microstructural constraints on the mechanisms of the transformation to reidite in naturally shocked zircon. *Contributions to Mineralogy and Petrology*, 172, 6.

Ferrière, L., Koeberl, C. & Reimold, W. (2009) Characterisation of ballen quartz and cristobalite in impact breccias: New observations and constraints on ballen formation. *European Journal of Mineralogy*, 21, 203–217.

Finch, R.J. & Hanchar, J.M. (2003) Structure and chemistry of zircon and zircon-group minerals. *Reviews in Mineralogy & Geochemistry*, 53, 1–25.

Fiske, P.S., Nellis, W.J. & Sinha, A.K. (1994) Shock-induced phase transitions of $ZrSiO_4$, reversion kinetics, and implications for terrestrial impact craters. *EOS Transactions*, 75.

French, B.M. (1998) *Traces of catastrophe: A handbook of shock-metamorphic effects in terrestrial meteorite impact structure*, LPI Contribution No. 954. Houston: Lunar and Planetary Institute.

French, B.M. & Koeberl, C. (2010) The convincing identification of terrestrial meteorite impact structures: What works, what doesn't, and why. *Earth-Science Reviews*, 98, 123–170.

Fritz, J., Assis Fernandes, V., Greshake, A., Holzwarth, A. & Böttger, U. (2019) On the formation of diaplectic glass: Shock and thermal experiments with plagioclase of different chemical

compositions. *Meteoritics & Planetary Science*, 54, 1533–1547.

Furukawa, Y., Nakazawa, H., Sekine, T., Kobayashi, T. & Kakegawa, T. (2015) Nucleobase and amino acid formation through impacts of meteorites on the early ocean. *Earth and Planetary Science Letters*, 429, 216–222.

Glass, B.P. & Liu, S. (2001) Discovery of high-pressure $ZrSiO_4$ polymorph in naturally occurring shock-metamorphosed zircons. *Geology*, 29, 371–373.

Glass, B.P. & Simonson, B.M. (2012) Distal impact ejecta layers: Spherules and more. *Elements*, 8, 43–48.

Glavin, D.P., Dworkin, J.P., Alexander, C.M.O.D., Aponte, J.C., Baczynski, A.A., Barnes, J.J., Bechtel, H.A., Berger, E.L., Burton, A.S., Caselli, P., Chung, A.H., Clemett, S.J., Cody, G.D., Dominguez, G., Elsila, J.E., Farnsworth, K.K., Foustoukos, D.I., Freeman, K.H., Furukawa, Y., Gainsforth, Z., Graham, H.V., Grassi, T., Giuliano, B.M., Hamilton, V.E., Haenecour, P., Heck, P.R., Hofmann, A.E., House, C.H., Huang, Y., Kaplan, H.H., Keller, L.P., Kim, B., Koga, T., Liss, M., McLain, H.L., Marcus, M.A., Matney, M., McCoy, T.J., McIntosh, O.M., Mojarro, A., Naraoka, H., Nguyen, A.N., Nuevo, M., Nuth, J.A., Oba, Y., Parker, E.T., Peretyazhko, T.S., Sandford, S.A., Santos, E., Schmitt-Kopplin, P., Seguin, F., Simkus, D.N., Shahid, A., Takano, Y., Thomas-Keprta, K.L., Tripathi, H., Weiss, G., Zheng, Y., Lunning, N.G., Righter, K., Connolly, H.C. & Lauretta, D.S. (2025) Abundant ammonia and nitrogen-rich soluble organic matter in samples from asteroid (101955) Bennu. *Nature Astronomy*, 9, 199–210.

Grieve, R.A.F., Langenhorst, F. & Stöffler, D. (1996) Shock metamorphism of quartz in nature and experiment: II. Significance in geoscience. *Meteoritics & Planetary Science*, 31, 6–35.

Hazen, R.M. & Finger, L.W. (1979) Crystal structure and compressibility of zircon at high pressure. *American Mineralogist*, 64, 196–201.

Hemley, R.J. (1987) Pressure dependence of Raman spectra of SiO_2 polymorphs: α-quartz, coesite, and stishovite. In *High-Pressure Research in Mineral Physics: A Volume in Honor of Syun-iti Akimoto*.

Holm-Alwmark, S., Rae, A.S.P., Ferrière, L., Alwmark, C. & Collins, G.S. (2017) Combining shock barometry with numerical modeling: Insights into complex crater formation—The example of the Siljan impact structure (Sweden). *Meteoritics & Planetary Science*, 52, 2521–2549.

Holm, S., Alwmark, C., Alvarez, W. & Schmitz, B. (2011) Shock barometry of the Siljan impact structure, Sweden. *Meteoritics & Planetary Science*, 46, 1888–1909.

Hoskin, P.W.O. (2005) Trace-element composition of hydrothermal zircon and the alteration of Hadean zircon from the Jack Hills, Australia. *Geochimica et Cosmochimica Acta*, 69, 637–648.

Hoskin, P.W.O. & Schaltegger, U. (2003) The composition of zircon and igneous and metamorphic petrogenesis. (*Note: If this is a book chapter or article, full source info is needed.*)

Kaiser, A., Lobert, M. & Telle, R. (2008) Thermal stability of zircon ($ZrSiO_4$). *Journal of the European Ceramic Society*, 28, 2199–2211.

Kamo, S.L. & Krogh, T.E. (1995) Chicxulub crater source for shocked zircon crystals from the Cretaceous–Tertiary boundary layer, Saskatchewan: Evidence from new U–Pb data. *Geology*, 23, 281–284.

Kamo, S.L., Reimold, W.U., Krogh, T.E. & Colliston, W.P. (1996) A 2.023 Ga age for the Vredefort impact event and a first report of shock metamorphosed zircons in pseudotachylitic breccias and granophyre. *Earth and Planetary Science Letters*, 144, 369–387.

Kenkmann, T., Poelchau, M.H. & Wulf, G. (2014) Structural geology of impact craters. *Journal of Structural Geology*, 62, 156–182

Kieffer, S.W. & Simonds, C.H. (1980) The role of volatiles and lithology in the impact cratering process. *Reviews of Geophysics*, 18, 143–181.

Koeberl, C. (2002) Mineralogical and geochemical aspects of impact craters. *Mineralogical Magazine*, 66, 745–768.

Koga, T. & Naraoka, H. (2017) A new family of extraterrestrial amino acids in the Murchison meteorite. *Scientific Reports*, 7, 636.

Kovaleva, E., Kusiak, M.A., Kenny, G.G., Whitehouse, M.J., Habler, G., Schreiber, A. & Wirth, R. (2021) Nano-scale investigation of granular neoblastic zircon, Vredefort impact structure, South Africa: Evidence for complete shock melting. *Earth and Planetary Science Letters*, 565, 116948.

Kraut, F. (1969) Über ein neues Impaktit-Vorkommen in Gebeite von Rochechouart, Chassenon. *Geol. Bavarica*, 61, 428.

Kraut, F. & French, B.M. (1971) The Rochechouart meteorite impact structure, France: Preliminary geological results. *Journal of Geophysical Research (1896–1977)*, 76, 5407–5413.

Krogh, T.E., Davis, D.W. & Corfu, F. (1984) Precise U–Pb zircon and baddeleyite ages for the Sudbury area. In: *The Geology and Ore Deposits of the Sudbury Structure*, edited by E.G. Pye, A.J. Naldrett & P.E. Giblin. Ontario Geological Survey Special Volume.

Krogh, T.E. & Davis, G.L. (1975) Alteration in zircons and differential dissolution of altered and metamict zircon. *Carnegie Institution of Washington Yearbook*, 74, 619–623.

Krogh, T.E., Kamo, S.L., Sharpton, V.L., Marin, L.E. & Hildebrands, A.R. (1993) U–Pb ages of single

shocked zircons linking distal K/T ejecta to the Chicxulub crater. *Nature*, 366, 731–734.

Kusaba, K., Syono, Y., Kikuchi, M. & Fukuoka, K. (1985) Shock behavior of zircon: Phase transition to scheelite structure and decomposition. *Earth and Planetary Science Letters*, 72, 433–439.

Kusaba, K., Yagi, T., Kikuchi, M. & Syono, Y. (1986) Structural considerations on the mechanism of the shock-induced zircon–scheelite transition in $ZrSiO_4$. *Journal of Physics and Chemistry of Solids*, 47, 675–679.

Lambert, P. (1977) The Rochechouart crater: Shock zoning study. *Earth and Planetary Science Letters*, 35, 258–268.

Lambert, P. (2010) Target and impact deposits at Rochechouart impact structure, France. (*Note: Please provide publication source if available—e.g., report, journal, or book chapter.*)

Langenhorst, F. & Deutsch, A. (2012) Shock metamorphism of minerals. *Elements*, 8, 31–36.

Leroux, H., Reimold, W.U., Koeberl, C., Hornemann, U. & Doukhan, J.C. (1999) Experimental shock deformation in zircon: A transmission electron microscopic study. *Earth and Planetary Science Letters*, 169, 291–301.

Line, M.A. (2007) Panspermia in the context of the timing of the origin of life and microbial phylogeny. *International Journal of Astrobiology*, 6, 249–254.

Marqués, M., Contreras-García, J., Flórez, M. & Recio, J.M. (2008) On the mechanism of the zircon–reidite pressure-induced transformation. *Journal of Physics and Chemistry of Solids*, 69, 2277–2280.

Melosh, H.J. (1989) *Impact Cratering: A Geologic Process*. Oxford University Press, New York, NY.

Meyer, C., Williams, I.S. & Compston, W. (1996) Uranium–lead ages for lunar zircons: Evidence for a prolonged period of granophyre formation from 4.32 to 3.88 Ga. *Meteoritics & Planetary Science*, 31, 370–387.

Ming, Z., Ekhard, K.H.S., Ian, F., Ann, G.-B., Philippe, D., Rodney, C.E., Andrew, M.C. & Hugues, L. (2000) Metamictization of zircon: Raman spectroscopic study. *Journal of Physics: Condensed Matter*, 12, 1915.

Mojzsis, S.J., Harrison, T.M. & Pidgeon, R.T. (2001) Oxygen-isotope evidence from ancient zircons for liquid water at the Earth's surface 4,300 Myr ago. *Nature*, 409, 178–181.

Moser, D.E., Cupelli, C.L., Barker, I., Flowers, R.M., Bowman, J.R., Wooden, J. & Hart, J.R. (2011) New zircon shock phenomena and their use for dating and reconstruction of large impact structures revealed by electron nanobeam (EBSD, CL, EDS) and isotopic U–Pb and (U–Th)/He analysis of the Vredefort dome. *Canadian Journal of Earth Sciences*, 48, 117–139.

O'Neill, C., Marchi, S., Zhang, S. & Bottke, W. (2017) Impact-driven subduction on the Hadean Earth. *Nature Geoscience*, 10, 793–797.

Osinski, G.R. & Ferrière, L. (2016) Shatter cones: (Mis)understood? *Science Advances*, 2, e1600616.

Osinski, G.R., Grieve, R.A.F., Ferrière, L., Losiak, A., Pickersgill, A.E., Cavosie, A.J., Hibbard, S.M., Hill, P.J.A., Bermudez, J.J., Marion, C.L., Newman, J.D. & Simpson, S.L. (2022) Impact Earth: A review of the terrestrial impact record. *Earth-Science Reviews*, 232, 104112.

Osinski, G.R. & Pierazzo, E. (2013) *Impact Cratering: Processes and Products*. Chichester, West Sussex: John Wiley & Sons.

Osinski, G.R., Tornabene, L.L., Banerjee, N.R., Cockell, C.S., Flemming, R., Izawa, M.R.M., McCutcheon, J., Parnell, J., Preston, L.J., Pickersgill, A.E., Pontefract, A., Sapers, H.M. & Southam, G. (2013) Impact-generated hydrothermal systems on Earth and Mars. *Icarus*, 224, 347–363.

Plan, A., Kenny, G.G., Erickson, T.M., Lindgren, P., Alwmark, C., Holm-Alwmark, S., Lambert, P., Scherstén, A. & Söderlund, U. (2021) Exceptional preservation of reidite in the Rochechouart impact structure, France: New insights into shock deformation and phase transition of zircon. *Meteoritics & Planetary Science*, 56, 1795–1828.

Pontefract, A., Osinski, G.R., Cockell, C.S., Moore, C.A., Moores, J.E. & Southam, G. (2014) Impact-generated endolithic habitat within crystalline rocks of the Haughton impact structure, Devon Island, Canada. *Astrobiology*, 14, 522–533.

Rae, A.S.P., Poelchau, M.H. & Kenkmann, T. (2021) Stress and strain during shock metamorphism. *Icarus*, 370, 114687.

Rasmussen, C., Stockli, D.F., Erickson, T.M. & Schmieder, M. (2020) Spatial U–Pb age distribution in shock-recrystallized zircon – A case study from the Rochechouart impact structure, France. *Geochimica et Cosmochimica Acta*, 273, 313–330.

Reddy, S.M., Johnson, T.E., Fischer, S., Rickard, W.D.A. & Taylor, R.J.M. (2015) Precambrian reidite discovered in shocked zircon from the Stac Fada impactite, Scotland. *Geology*, 43, 899–902.

Reid, A.F. & Ringwood, A.E. (1969) Newly observed high-pressure transformations in Mn_3O_4, $CaAl_2O_4$, and $ZrSiO_4$. *Earth and Planetary Science Letters*, 6, 205–208.

Robbins, S.J. & Hynek, B.M. (2012) A new global database of Mars impact craters ≥1 km: 1. Database creation, properties, and parameters. *Journal of Geophysical Research: Planets*, 117.

Rocca, M.C.L., Rampino, M.R. & Báez Presser, J.L. (2017) Geophysical evidence for a large impact structure on the Falkland (Malvinas) Plateau. *Terra Nova*, 29, 233–237.

Sapers, H.M., Osinski, G.R., Banerjee, N.R., Ferrière, L., Lambert, P. & Izawa, M.R.M. (2014) Revisiting the Rochechouart impact structure, France. *Meteoritics & Planetary Science*, 49, 2152–2168.

Sarli, B., Bowman, E., Cataldo, G., Feehan, B., Green, T., Gough, K., Hagedorn, A., Hudgins, P., Lin, J., Neuman, M., Parvez, E., Rondey, J., Szalai, C. & Yew, C. (2024) NASA's Capture, Containment, and Return System: Bringing Mars samples to Earth. *Acta Astronautica*, 223, 270–303.

Schmieder, M., Buchner, E., Schwarz, W.H., Trieloff, M. & Lambert, P. (2010) A Rhaetian $^{40}Ar/^{39}Ar$ age for the Rochechouart impact structure (France) and implications for the latest Triassic sedimentary record. *Meteoritics & Planetary Science*, 45, 1225–1242.

Schmieder, M. & Kring, D.A. (2020) Earth's impact events through geologic time: A list of recommended ages for terrestrial impact structures and deposits. *Astrobiology*, 20, 91–141.

Shkolyar, S., Jaret, S.J., Cohen, B.A., Johnson, J.R., Beyssac, O., Madariaga, J.M., Wiens, R.C., Ollila, A., Holm-Alwmark, S. & Liu, Y. (2022) Identifying shocked feldspar on Mars using Perseverance spectroscopic instruments: Implications for geochronology studies on returned samples. *Earth, Moon, and Planets*, 126, 4.

Sieh, K., Herrin, J., Jicha, B., Schonwalder Angel, D., Moore, J.D.P., Banerjee, P., Wiwegwin, W., Sihavong, V., Singer, B., Chualaowanich, T. & Charusiri, P. (2020) Australasian impact crater buried under the Bolaven volcanic field, Southern Laos. *Proceedings of the National Academy of Sciences*, 117, 1346.

Simonson, B.M. & Glass, B.P. (2004) Spherule layers—Records of ancient impacts. *Annual Review of Earth and Planetary Sciences*, 32, 329–361.

Söderlund, U. & Johansson, L. (2002) A simple way to extract baddeleyite (ZrO_2). (*Note: Publication source is missing—please provide journal/book info to complete citation.*)

Spray, J.G., Kelley, S.P. & Rowley, D.B. (1998) Evidence for a late Triassic multiple impact event on Earth. *Nature*, 392, 171–173.

Stöffler, D. (1971) Progressive metamorphism and classification of shocked and brecciated crystalline rocks at impact craters. *Journal of Geophysical Research (1896–1977)*, 76, 5541–5551.

Stöffler, D. (1972) Deformation and transformation of rock-forming minerals by natural and experimental shock processes. I. Behavior of minerals under shock compression. *Fortschritte der Mineralogie*, 49, 50–113.

Stöffler, D. (1984) Glasses formed by hypervelocity impact. *Journal of Non-Crystalline Solids*, 67, 465–502.

Stöffler, D., Hamann, C. & Metzler, K. (2018) Shock metamorphism of planetary silicate rocks and sediments: Proposal for an updated classification system. *Meteoritics & Planetary Science*, 53, 5–49.

Stöffler, D., and Grieve, R., 2007, Impactites, Chapter 2.11 in Fettes, D. and Desmons, J. (eds.) Metamorphic Rocks: A Classification and Glossary of Terms, Recommendations of the International Union of Geological Sciences, Cambridge, UK, Cambridge University Press. 82-92, 111-125, and 126-242

Szumila, I., Trail, D., Erickson, T., Simon, J.I., Wielicki, M.M., Lapen, T., Nakajima, M., Fries, M. & Bell, E.A. (2023) Microstructural changes and Pb mobility during the zircon to reidite transformation: Implications for planetary impact chronology. *American Mineralogist*, 108, 1516–1529.

Takeuchi, Y., Furukawa, Y., Kobayashi, T., Sekine, T., Terada, N. & Kakegawa, T. (2020) Impact-induced amino acid formation on Hadean Earth and Noachian Mars. *Scientific Reports*, 10, 9220.

Tarduno, J.A., Cottrell, R.D., Davis, W.J., Nimmo, F. & Bono, R.K. (2015) A Hadean to Paleoarchean geodynamo recorded by single zircon crystals. *Science*, 349, 521–524.

Timms, N.E., Erickson, T.M., Pearce, M.A., Cavosie, A.J., Schmieder, M., Tohver, E., Reddy, S.M., Zanetti, M.R., Nemchin, A.A. & Wittmann, A. (2017a) A pressure–temperature phase diagram for zircon at extreme conditions. *Earth-Science Reviews*, 165, 185–202.

Timms, N.E., Erickson, T.M., Zanetti, M.R., Pearce, M.A., Cayron, C., Cavosie, A.J., Reddy, S.M., Wittmann, A. & Carpenter, P.K. (2017b) Cubic zirconia in >2370 °C impact melt records Earth's hottest crust. *Earth and Planetary Science Letters*, 477, 52–58.

Timms, N.E., Reddy, S.M., Healy, D., Nemchin, A.A., Grange, M.L., Pidgeon, R.T. & Hart, R. (2012) Resolution of impact-related microstructures in lunar zircon: A shock-deformation mechanism map. *Meteoritics & Planetary Science*, 47, 120–141.

Tissot, F.L.H., Ibanez-Mejia, M., Boehnke, P., Dauphas, N., McGee, D., Grove, T.L. & Harrison, T.M. (2019) $^{238}U/^{235}U$ measurement in single-zircon crystals: Implications for the Hadean environment, magmatic differentiation and geochronology. *Journal of Analytical Atomic Spectrometry*, 34, 2035–2052.

Trepmann, C.A. (2008) Shock effects in quartz: Compression versus shear deformation — An example from the Rochechouart impact structure, France. *Earth and Planetary Science Letters*, 267, 322–332.

Valley, J.W., Cavosie, A.J., Ushikubo, T., Reinhard, D.A., Lawrence, D.F., Larson, D.J., Clifton, P.H., Kelly, T.F., Wilde, S.A., Moser, D.E. & Spicuzza,

M.J. (2014) Hadean age for a post-magma-ocean zircon confirmed by atom-probe tomography. *Nature Geoscience*, 7, 219–223.

Williams, D.B. & Carter, C.B. (2009) The transmission electron microscope. In: Williams, D.B. & Carter, C.B. (eds.) *Transmission Electron Microscopy: A Textbook for Materials Science*. Boston, MA: Springer US.

Wirth, R. (2009) Focused ion beam (FIB) combined with SEM and TEM: Advanced analytical tools for studies of chemical composition, microstructure and crystal structure in geomaterials on a nanometre scale. *Chemical Geology*, 261, 217–229.

Wittmann, A., Kenkmann, T., Schmitt, R.T. & Stöffler, D. (2006) Shock-metamorphosed zircon in terrestrial impact craters. *Meteoritics & Planetary Science*, 41, 433–454.

Woodhead, J.A., Rossman, G.R. & Silver, L.T. (1991) The metamictization of zircon: Radiation dose-dependent structural characteristics. *American Mineralogist*, 76, 74–82.

Yada, T., Abe, M., Okada, T., Nakato, A., Yogata, K., Miyazaki, A., Hatakeda, K., Kumagai, K., Nishimura, M., Hitomi, Y., Soejima, H., Yoshitake, M., Iwamae, A., Furuya, S., Uesugi, M., Karouji, Y., Usui, T., Hayashi, T., Yamamoto, D., Fukai, R., Sugita, S., Cho, Y., Yumoto, K., Yabe, Y., Bibring, J.-P., Pilorget, C., Hamm, V., Brunetto, R., Riu, L., Lourit, L., Loizeau, D., Lequertier, G., Moussi-Soffys, A., Tachibana, S., Sawada, H., Okazaki, R., Takano, Y., Sakamoto, K., Miura, Y.N., Yano, H., Ireland, T.R., Yamada, T., Fujimoto, M., Kitazato, K., Namiki, N., Arakawa, M., Hirata, N., Yurimoto, H., Nakamura, T., Noguchi, T., Yabuta, H., Naraoka, H., Ito, M., Nakamura, E., Uesugi, K., Kobayashi, K., Michikami, T., Kikuchi, H., Hirata, N., Ishihara, Y., Matsumoto, K., Noda, H., Noguchi, R., Shimaki, Y., Shirai, K., Ogawa, K., Wada, K., Senshu, H., Yamamoto, Y., Morota, T., Honda, R., Honda, C., Yokota, Y., Matsuoka, M., Sakatani, N., Tatsumi, E., Miura, A., Yamada, M., Fujii, A., Hirose, C., Hosoda, S., Ikeda, H., Iwata, T., Kikuchi, S., Mimasu, Y., Mori, O., Ogawa, N., Ono, G., Shimada, T., Soldini, S., Takahashi, T., Takei, Y., Takeuchi, H., Tsukizaki, R., Yoshikawa, K., Terui, F., Nakazawa, S., Tanaka, S., Saiki, T., Yoshikawa, M., et al. (2022) Preliminary analysis of the Hayabusa2 samples returned from C-type asteroid Ryugu. *Nature Astronomy*, 6, 214–220.

Yang, C., Zhao, H., Bruzzone, L., Benediktsson, J.A., Liang, Y., Liu, B., Zeng, X., Guan, R., Li, C. & Ouyang, Z. (2020) Lunar impact crater identification and age estimation with Chang'E data by deep and transfer learning. *Nature Communications*, 11, 6358.

Papers published in refereed journals, and extended conference abstracts not included in this thesis

Hyde, W. R., Jaret, S. J., Kenny, G. G., **Plan, A.**, Rugen, E. J., Whitehouse, M. J., Alwmark, S. (2025). *First radioisotopic age constraints of the Cambrian Ritland impact structure, Norway.* Manuscript in review in Meteoritics and Planetary Science.

Hyde, W. R., Kenny, G. G., Whitehouse, M. J., Wirth, R., Roddatis, V., Schreiber, A., Garde, A. A., **Plan, A.**, Larsen, N. K. (2024). *Microstructural and isotopic analysis of shocked monazite from the Hiawatha impact structure: development of porosity and its utility in dating impact craters*. Contributions to Mineral Petrology 179, 28.

Plan, A., Kenny, G. G., Erickson, T. M., Hyde, W. R., Alwmark, S., Söderlund, U. (2024). *Tracing Geochemical Pattern of Zircon → Reidite → Zircon Phase Transitioning.* 87th Annual Meeting of The Meteoritical Society. Abstract #6345.

Alwmark, S., Alwmark, C., Wallentin, J., Hektor, J., Chen, H., Gajewska, K., Kalbfleisch, S., Lidin, S., **Plan, A.**, Struzynska, P., & Langenhorst, F. *Spatially resolved planar deformation features in naturally and experimentally shocked quartz with synchrotron X-ray diffraction.* 86th Annual Meeting of The Meteoritical Society. Abstract #6316.

Urueña, C. L., Möller, C., **Plan, A.** (2023). *Metamorphic titanite–zircon pseudomorphs after igneous zirconolite*, European Journal of Mineralogy, 35, 773–788.

Plan, A., Alwmark, S., Erickson, T. M., Söderlund, U. (2023). *Characteristic Raman Spectra of Various Reidite Habits and FRIGN Zircon.* 86th Annual Meeting of The Meteoritical Society. Abstract #6132.

Kring, D. A., Bamber, E., Blance, A., Bretzfelder, J., Faucher, J., Flom, A., Franco, K. L., Harris, E., Jhoti, E., Laferriere, K., Martin, A., Meyer, M., Pamerleau, I., **Plan, A.**, Roberts, E., Shubham, S., Slumba, K., Zimmermann, N., and Barrett, T. (2023). *Cascading boulder and boulder track experiment at barringer meteorite crater (aka meteor crater), Arizona.* 54th Lunar and Planetary Science Conference. Abstract #2186.

Plan, A., Lindgren, P., Erickson, T. M., Söderlund, U. (2022). *Reidite discovered in the Triassic distal impact ejecta deposit of southwest Britain.* 85th Annual Meeting of The Meteoritical Society. Abstract #6280.

Lindgren, P., Hallis, L., Hage, F.S., Lee, M.R., Parnell, J., **Plan, A.**, Doye, A., MacLaren, I. (2019), *A TEM and EELS study of carbon in a melt fragment from the Gardnos impact structure*. Meteoritics and Planetary Science, 54: 2698-2709.

Svensk sammanfattning

Sedan mitten av 1900-talet har synen på kollisioner mellan himmlakroppar förändrats radikalt. Från att ha betraktats som kuriositeter har desa processer kommit att erkännas som fundamentala för planeternas utveckling, och på jorden, för livets uppkomst och dess evolution. Idag vet vi att utav alla geologiska formationer som präglar det inre solsystemets stengia planeter, och dess månar, är nedslagskratrar de mest utbredda strukturerna. På månen framträder det kosmiska bombardemanget tydligt, vars yta täcks utav tusentals nedslagskratrar. Vid en första anblick utav vår planets yta är dock dessa formationer inte lika framträdanden. Förklaringen ligger i att Månen är en relativt passiv geologisk himmlakropp, medan Jorden präglas utav geologiska processer som ständigt omformar vår planet. Dessa processer, som till exempel plattektonik, sedimentation och erosion, har över geologisk tid bidragit till att antingen begrava eller fullständigt radera de tidigare spår utav meteoritnedslag. Som följd av dessa geologiska processer är bevarelsegraden impaktstrukturer väldigt låg, idag känner vi endast till ca. 200 nedslagstrukturer på jorden. Genom studiera utav dessa strukturer vet vi idag att meteoritnedslag kan leda till dramatiska och omfattande konsekvenser. Det mest kända exemplet tillskrivs den cirka 10 kilometer stora asteroiden som träffade Yucatánhalvön för 66 miljoner år sedan. Tidpunkten för nedslaget sammanfaller med det massutdöende som bland annat avslutade dinosauriernas dominans. När en himlakropp slår ner i jordskorpan frigörs enorma energier. I denna explosion uppstår enorma tryck och temperaturer som kraftigt överstiger de förhållanden som uppnås vid mer vanliga geologiska processer i jordens inre. Vid nedslaget bildas chockvågor vilket medför omedelbara och permanenta förändringar i berggrunden. Detta ger i sin tur upphov till säregna mineralogiska och mikrostrukturella signaturer som endast kan bildas under så kallad chockmetamorfos—en geologisk process diagnotiskt för dom höga tryck-temperatur förhållanden som förkommer vid nedslag. Att studera nedslagskratrar är avgörande för att förstå både jordens geologiska utveckling och livets historia. Dessa strukturer fungerar som arkiv över katastrofala händelser som inte bara omformat landskapet, utan också styrt evolutionens riktning, från livets utveckling till däggdjurens herravälde. Genom att kartlägga och åldersbestämma dessa strukturer kan vi inte bara rekonstruera solsystemets våldsamma förflutna, utan även förstå oss på dessa grundläggande processer bättre.

I denna avhandling undersöks hur mineralet zirkon påverkas av de extrema tryck-temperaturförhållanden som uppstår vid meteoritnedslag. Zirkon är ett av de mest motståndskraftiga mineralen i jordskorpan, och är särskilt intressant eftersom mineralet kan användas för att åldersbestämma geologiska processer. Denna datering genoförs genom mätningar utav zirkonets naturliga ”klocka”, vilket styrs utav sönderfallet från uran (U) till bly (Pb). När zirkon exponeras för de extrema tryck och temperaturer kan mineralet genomgå unika mikrostrukturella förändringar, bland annat genom fasövergång till sin högtrycksfas reidit (likt hur kol blir diamant vid höga tryck), samt omkristallisera vid extrema temperaturer. Detta kan leda till att spårelement mobilisera och därmed kan zirkonets U-Pb ”klocka” genomgå modifikationer. Forskningsresultaten som presenteras i denna avhandling ger en inblick och utökad förståelse kring det deformationsmekanismerna som ligger bakom omvandling från zirkon till reidit och dess bevarandepotential, samt hur omkristalliserings-processen sker. Genom mikroanalytiska metoder som svepelektron-mikroskopi, *electron backscatter diffraction* (EBSD) och Ramanspektroskopi har zirkonkorn undersökts från Rochechouart-nedslagsstrukturen i Frankrike, en av Europas största nedslagskratrar.

Avhandlingens studier bidrar till en fördjupad förståelse av hur zirkon och dess kristallstruktur reagerar på chockdeformation vid meteoritnedslag. Resultaten ger nya verktyg för att tolka tryck- och temperaturförhållanden i samband med chock-inducerad omvandling. Upptäckten av tidigare okända reiditemorfologier och omkristallisationstexturer som här presenteras, samt hur Raman data från zirkon kan bättre tolkas, stärker zirkonets roll som indikator för nedslagshändelser. Dessa fynd kan även vara till hjälp vid åldersbestämning av nedslagskratrar, då de möjliggör en mer tillförlitlig tolkning av tryck-temperaturhistorik, samt huruvida U-Pb-systemet påverkats. Sammantaget förbättrar resultaten vår

förståelse för de processer som påverkar zirkon vid nedslag—hur reidite bildas, bevaras eller omvandlas—och hur chockinducerad omkristallisation fungerar på mikroskopisk nivå.

Litholund Theses

Dissertations

1. *Emma F. Rehnström,* 2003: Geography and geometry of pre-Caledonian western Baltica: U-Pb geochronology and palaeomagnetism.

2. *Oskar Paulsson,* 2003: U-Pb geochronology of tectonothermal events related to the Rodinia and Gondwana supercontinents: observations from Antarctica and Baltica.

3. *Ingela Olsson-Borell,* 2003: Thermal history of the Phanerozoic sedimentary succession of Skåne, southern Sweden, and implications for applied geology.

4. *Johan Lindgren,* 2004: Early Campanian mosasaurs (Reptilia; Mosasauridae) from the Kristianstad Basin, southern Sweden.

5. *Audrius Cecys,* 2004: Tectonic implications of the ca. 1.45 Ga granitoid magmatism at the southwestern margin of the East European Craton.

6. *Peter Dahlqvist,* 2005: Late Ordovician-Early Silurian facies development and stratigraphy of Jämtland, central Sweden.

7. *Mårten Eriksson,* 2005: Silurian carbonate platform and unconformity development, Gotland, Sweden.

8. *Jane Wigforss-Lange,* 2005: The effects of Late Silurian (mid-Ludfordian) sea-level change: a case study of the Öved-Ramsåsa Group in Skåne, Sweden.

9. *Erik Eneroth,* 2006: Nanomagnetic and micromagnetic properties of rocks, minerals and sulphide-oxidation products.

10. *Niklas Axheimer,* 2006: The lower and middle Cambrian of Sweden: trilobites, biostratigraphy and intercontinental correlation.

11. *Fredrik Terfelt,* 2006: Upper middle Cambrian through Furongian of Scandinavia with focus on trilobites, paleoenvironments and correlations.

12. *Andrius Rimsa,* 2007: Understanding zircon geochronology: constraints from imaging and trace elements.

13. *Mårten Eriksson* 2007: Silurian carbonate platforms of Gotland, Sweden: archives of local, regional and global environmental changes.

14. *Jane Wigforss-Lange,* 2007: Geochemical and sedimentary signatures of Phanerozoic events.

15. *Tobias Hermansson,* 2007: The tectonic evolution of the western part of the Svecofennian orogen, central Sweden: Insight from U/Pb and $^{40}Ar/^{39}Ar$ geochronology at Forsmark.

16. *Pia Söderlund,* 2008: ^{40}Ar-^{39}Ar, AFT and (U-Th)/He thermochronologic implications for the low-temperature geological evolution in SE Sweden.

17. *Anders Cronholm,* 2009: The flux of extraterrestrial matter to Earth as recorded in Paleogene and Middle Ordovician marine sediments.

18. *Carl Alwmark,* 2009: Traces in Earth's geological record of the break-up of the L-chondrite parent body 470 Ma.

19. *Linda Larsson-Lindgren,* 2009: Climate and vegetation during the Miocene: evidence from Danish palynological assemblages.

20. *Ingemar Bergelin,* 2010: $^{40}Ar/^{39}Ar$ whole-rock geochronology of Mesozoic basalts in Scania: evidence for episodic volcanism over an extended period of ca. 80 Myr.

21. *Johanna Mellgren,* 2011: Conodont biostratigraphy, taxonomy and palaeoecology in the Darriwilian (Middle Ordovician) of Baltoscandia: with focus on meteorite and extraterrestrial chromite-rich strata.

22. *Johan Olsson,* 2012: U-Pb baddeleyite geochronology of Precambrian mafic dyke swarms and complexes in southern Africa: regional-scale extensional events and the origin of the Bushveld complex.

23. *Kristina Mehlqvist,* 2013: Early land plant spores from the Paleozoic of Sweden : taxonomy, stratigraphy and paleoenvironments.

24. *Andreas Petersson,* 2015: Evolution of continental crust in the Proterozoic: growth and reworking in orogenic systems.

25. *Karolina Bjärnborg,* 2015: Origin of the Kleva Ni-Cu sulphide mineralisation in Småland, southeast Sweden.

26. *Lorraine Tual,* 2016: P–T evolution and high-temperature deformation of Precambrian eclogite, Sveconorwegian orogen.

27. *Mimmi Nilsson,* 2016: New constraints on paleoreconstructions through geochronology of mafic dyke swarms in North Atlantic Craton.

28. *Sanna Alwmark,* 2016: Terrestrial consequences of hypervelocity impact: shock metamorphism, shock barometry, and newly discovered impact structures.

29. *Anders Lindskog,* 2017: Early–Middle Ordovician biotic and sedimentary dynamics in the Baltoscandian paleobasin.

30. *Ashley Gumsley*, 2017: Validating the existence of the supercraton Vaalbara in the Mesoarchaean to Palaeoproterozoic.

31. *Johan Gren,* 2018: Molecular, micro- and ultrastructural investigations of labile tissues in deep time.

32. *Elisabeth Einarsson,* 2018: Palaeoenvironments, palaeoecology and palaeobiogeography of Late Cretaceous (Campanian) faunas from the Kristianstad Basin, southern Sweden, with applications for science education.

33. *Victoria Beckman,* 2018: Metamorphic zircon formation in gabbroic rocks: the tale of microtextures.

34. *Maria Herrmann,* 2020: Geochronology of impact structures - constraining syn- and post-impact processes using the $^{40}Ar/^{39}Ar$ and U-Pb techniques.

35. *Miriam Heingård,* 2022: Exceptional fossil preservation: implications for palaeobiology and taphonomy.

36. *Randolph De La Garza*, 2022: Preservation of Marine Reptile Soft Parts: Reconstructing the Life and Death of Ancient Leviathans.

37. *Josefin Martell*, 2022: Leave no trace: A non-destructive correlative approach providing new insights into impactites and meteorites.

38. *Cindy Urueña*, 2023: Metamorphism in the roots of mountain belts and its effect on rock technical properties: A case study of the Eastern Segment, Sveconorwegian orogeny.

39. *Ingrid Urban*, 2023: Marine oolites as proxies for palaeoenvironmental reconstructions during extinction events.

40. *Tjördis Störling*, 2024: Changes in ocean geochemistry across the K- Pg boundary interval.

41. *Karolina Brylka*, 2024: Origin and the evolution of diatoms through the integration of paleontology and phylogenetics.

42. *Anders Plan*, 2025: Microstructural Deformation of Zircon During Impact Metamorphism.